

1 Global 1km Land Surface Parameters for Kilometer-Scale Earth System Modeling

2 Lingcheng Li, Gautam Bisht, Dalei Hao, L. Ruby Leung

3 Atmospheric, Climate, and Earth Sciences Division, Pacific Northwest National Laboratory,
4 Richland, WA, USA

5

6 Correspondence: Lingcheng Li (lingcheng.li@pnnl.gov) and Gautam Bisht
7 (gautam.bisht@pnnl.gov)

8

9 **Abstract**

10 Earth system models (ESMs) are progressively advancing towards the kilometer scale (k-scale).
11 However, the surface parameters for Land Surface Models (LSMs) within ESMs running at the k-
12 scale are typically derived from coarse resolution and outdated datasets. This study aims to develop
13 a new set of global land surface parameters with a resolution of 1 km for multiple years from 2001
14 to 2020, utilizing the latest and most accurate available datasets. Specifically, the datasets consist
15 of parameters related to land use and land cover, vegetation, soil, and topography. Differences
16 between the newly developed 1k land surface parameters and conventional parameters emphasize
17 their potential for higher accuracy due to the incorporation of the most advanced and latest data
18 sources. To demonstrate the capability of these new parameters, we conducted 1 km resolution
19 simulations using the E3SM Land Model version 2 (ELM2) over the contiguous United States.
20 Our results demonstrate that land surface parameters contribute to significant spatial heterogeneity
21 in ELM2 simulations of soil moisture, latent heat, emitted longwave radiation, and absorbed
22 shortwave radiation. On average, about 31% to 54% of spatial information is lost by upscaling the
23 1 km ELM2 simulations to a 12 km resolution. Using eXplainable Machine Learning (XML)
24 methods, the influential factors driving the spatial variability and spatial information loss of ELM2
25 simulations were identified, highlighting the substantial impact of the spatial variability and
26 information loss of various land surface parameters, as well as the mean climate conditions. The
27 new land surface parameters are tailored to meet the emerging needs of k-scale LSMs and ESMs
28 modeling with significant implications for advancing our understanding of water, carbon, and
29 energy cycles under global change. The 1 km land surface parameters are publicly available at
30 <https://doi.org/10.25584/PNNLDH/1986308> (Li et al., 2023).

31 **1. Introduction**

32 Aided by advancements in computing power, it has become increasingly feasible to run land
33 surface models (LSMs) and Earth system models (ESMs) at the kilometer scale (k-scale) to
34 improve our understanding of Earth system processes. The emergence of k-scale modeling has the
35 potential to improve the accuracy of climate simulations significantly and allow for explicit
36 modeling of physical processes that were previously poorly represented in climate models (Nat.
37 Clim. Chang. 2022), such as modeling of mesoscale convective systems in the atmosphere (Slingo
38 et al., 2022) and mesoscale eddies in ocean (Hewitt et al., 2022). Simultaneously, land modeling
39 has also witnessed a surge of interest in hyper-resolution modeling, initially proposed by Wood et
40 al. (2011), which aims to model land surface processes at a horizontal resolution of 1 km globally
41 and 100 m or finer for continental or regional domains. The motivation behind hyper-resolution
42 modeling is to address the requirements of operational forecasting like extreme events, and to
43 enhance our understanding of hydrological and biogeochemical cycling, and land–atmosphere
44 interactions. High-resolution LSMs have been increasingly applied in various fields, as
45 demonstrated by recent examples, such as 30-meter soil moisture simulations over the contiguous
46 United States (CONUS) (Vergopolan et al., 2020, 2021, 2022), 500-meter hyper-resolution
47 modeling of surface and root zone soil moisture over Oklahoma (Rouf et al., 2021), 1-km
48 simulations over Southwestern US (Singh et al., 2015), 3-km simulations over eastern Tibetan
49 Plateau to understand hydrological changes over mountainous regions (Yuan et al., 2018; Ji and
50 Yuan, 2018), 6-km simulations over China to reduce simulations errors of hydrological variables
51 (Ji et al., 2023). High-resolution modeling can better capture the land surface heterogeneity and
52 could improve simulations of terrestrial water and energy cycles (Giorgi and Avissar, 1997;
53 Chaney et al., 2018; Xu et al., 2023), biogeochemical cycles (Chaney et al., 2018), as well as land–

54 atmosphere coupling (Liu et al., 2017; Zhou et al., 2019; Bou-Zeid et al., 2020). For example,
55 Singh et al. (2015) demonstrated that increasingly capturing topography and soil texture
56 heterogeneity at finer resolutions (e.g., 1 km) improves land surface modeling of water and energy
57 variables. Li et al. (2022) have shown that the spatial heterogeneities of land surface parameters
58 (including land use and land cover (LULC) and topography) are essential for modeling the spatial
59 variability of land surface energy and water partitioning. Hao et al. (2022) found that 1 km
60 simulations with sub-grid topographic configurations can better capture the topographic effects on
61 surface fluxes.

62

63 The parameters for LSMs within ESMs being run at the k-scale are typically derived from coarse
64 resolution datasets or outdated datasets. Consequently, k-scale modeling may not accurately
65 represent fine-scale land surface heterogeneity unless high-resolution land surface parameters at
66 the kilometer or finer scales are utilized. Publicly available land surface parameters are primarily
67 provided at coarse resolutions and based on outdated datasets (see details in Table 1). For example,
68 the Community Land Model version 5 (CLM5; Lawrence et al., 2019) typically relies on land
69 surface parameters with spatial resolutions ranging from 1km to 0.5° based on source datasets that
70 were processed more than 10 years ago (see Table 1 for details). Although LULC-related
71 parameters are available at a relatively high resolution of 0.05°, they are temporally static and were
72 derived from a combination of data from different years spanning 1993 to 2012 (Table 1). Leaf
73 area index (LAI) was derived from the now outdated products of Moderate Resolution Imaging
74 Spectroradiometer (MODIS) collection 4 (Myneni et al., 2002). The canopy height for tree Plant
75 Functional Types (PFTs) is based on forest canopy height data derived from the Geoscience Laser
76 Altimeter System (GLAS) aboard ICESat, collected in 2005 (Simard et al., 2011). Canopy height

77 for short vegetation is represented by PFT-specific values that remain invariant in space (Bonan et
78 al., 2002). Soil sand and clay content were obtained from the International Geosphere-Biosphere
79 Programme (IGBP) soil dataset (Global Soil Data Task 2000) consisting of 4931 soil mapping
80 units (IGBP, 2000). These CLM5 land surface parameters have been widely utilized in the LSMs
81 and ESMS communities, despite being developed over a decade ago. Subsequently, Ke et al. (2012;
82 hereafter referred to as K2012) developed an updated set of LULC and vegetation-related land
83 surface parameters for CLM4 at a resolution of 0.05°. These parameters were developed based on
84 MODIS collection 5 products or datasets derived from MODIS collection 5 products, including
85 PFTs and non-vegetation land cover, LAI, and Stem Area Index (SAI). K2012 has also been widely
86 used by LSMs, including CLM (e.g., Leng et al., 2013; Ke et al., 2013; Singh et al., 2015; Xia et
87 al., 2017) and the Energy Exascale Earth System Model (E3SM) Land Model (ELM) (e.g.,
88 Caldwell et al., 2019; Leung et al., 2020; Li et al., 2022). However, the CLM5 and K2012 datasets,
89 with their relatively coarse resolution and reliance on outdated data from over a decade ago, may
90 not fully meet the requirements for k-scale modeling. Additionally, these datasets include LULC,
91 LAI, and SAI that are year invariant. Consequently, they are inappropriate for studies involving
92 LULC changes, such as urbanization. In addition, some recently developed land surface processes
93 and their associated parameters are not included in previous datasets. For instance, Hao et al. (2021)
94 introduced a sub-grid topographic parameterization of solar radiation with five associated
95 topographic factors in ELM, which have been found to significantly affect the surface energy
96 budget. the surface energy budget.

97
98 High-resolution and up-to-date datasets at kilometer or finer resolutions are now widely available
99 and can be utilized to derive more accurate land surface parameters for k-scale LSM simulations.

100 For example, the MODIS Land Cover Type Collection 6 (MCD12Q1 C6) data product provides
101 global land cover types yearly from 2001 to the present (Friedl et al., 2019; Sulla-Menashe et al.,
102 2019) at 500-meter resolution. Compared to the MODIS Collection 4 (used in CLM5 land surface
103 parameters) and Collection 5 products (used in K2012 land surface parameters), the C6 data
104 represents a significant advancement in algorithm improvements and the quality of land cover
105 information. Despite the availability of high-resolution MODIS LAI products, such as the 500 m
106 MCD15A2H (Myneni et al., 2021), they suffer from noise and gaps with spatially and temporally
107 inconsistent values due to clouds, seasonal snow cover, instrument issues, and uncertainties in
108 retrieval algorithms (Yuan et al., 2011). To address these limitations, Yuan et al. (2011)
109 reprocessed MODIS LAI products and generated a more accurate and spatiotemporally continuous
110 and consistent LAI dataset that is available continuously to the present period. Additional high-
111 resolution and up-to-date datasets are available for preparing land surface parameters, such as soil
112 texture and soil organic matter at 250-meter resolution (Poggio et al., 2021) and vegetation height
113 at 10-m resolution (Lang et al., 2023).

114

115 This study aims to develop a new set of global land surface parameters with a resolution of 1 km
116 for multiple years, utilizing the latest and most accurate available datasets. These parameters will
117 be tailored to meet the needs of k-scale Earth system modeling. The newly developed land surface
118 parameters include four categories: (1) LULC-related parameters, such as the spatial distributions
119 of PFTs, lakes, wetlands, urban areas, and glaciers; (2) vegetation-related parameters, including
120 PFTs' LAI and SAI for multiple years ranging from 2001 to 2021, and the canopy top and bottom
121 height; (3) soil-related parameters, such as soil textures and soil organic matter; and (4)
122 topography-related parameters, such as elevation, slope, aspect, and sub-grid topographic factors.

123 We conducted a comparison of the new 1k parameters against the K2012 and ELM2/CLM5 default
124 parameters. Utilizing ELM version 2 (ELM2) as a testbed, we demonstrated the modeling
125 capability enabled by the new high-resolution parameters through a 5-year simulation at 1 km
126 resolution over the CONUS. We performed a spatial scaling analysis on four ELM2 simulated
127 variables, which included soil moisture, latent heat, emitted longwave radiation, and absorbed
128 shortwave radiation, to underscore the significance of high-resolution land surface parameters on
129 ELM2 simulations. We employed eXplainable Machine Learning (XML) methods to evaluate the
130 most important factors of land surface parameters and climate conditions (e.g., mean temperature
131 and precipitation) in driving the spatial variability and spatial information loss of ELM2
132 simulations.

133 **2. Development of 1km land surface parameters**

134 In this study, all the land surface parameters were developed globally at a resolution of
135 approximately 1 km (i.e., 1/120°, hereafter referred to as 1 km; Table 1). The LULC-related
136 parameters, soil properties, canopy height, and elevation were processed via Google Earth Engine
137 (GEE; Gorelick et al., 2017). The LAI was processed using an area-weighted average from its
138 original 450 m resolution obtained from Beijing Normal University (Yuan et al., 2011). All data
139 sources utilized in this study have been rigorously validated in their respective original
140 publications. The detailed methods for deriving these parameters are described below.

141

Table 1 Comparison between new and previous land surface parameters

Category	Land surface parameters	This study	ELM2 / CLM5 *	K2012
LULC	PFTs, Lake, Glacier, Urban	<ul style="list-style-type: none"> Resolution: 1 km, yearly, 2001-2020 Data source: 500 m, yearly, MODIS collection 6 (Friedl et al., 2019) 	<ul style="list-style-type: none"> Resolution: 0.05°, temporally static, processed based on data from mixed years PFTs data source: mixed years from 1993 to 2001; 500 m, MODIS Vegetation Continuous Fields (Hansen et al., 2003); 1 km, tree cover (Defries et al., 2000); 10 km (5 arc minutes), cropland (Ramankutty and Foley, 1999); 1 km, MODIS land cover collection 4 (Friedl et al., 2002) Lake data source: 3 km (90 arc seconds) lake data (Kourzeneva 2009, 2010) Glacier data source: glacier and ice sheet vector data (Arendt et al. 2012; Rastner et al. 2012) Urban data source: 1 km urban data (Jackson et al., 2010) 	<ul style="list-style-type: none"> Resolution: 0.05°, year 2005 Data source: 500 m, yearly, MODIS collection 5 (Friedl et al., 2010)
Vegetation	LAI, SAI	<ul style="list-style-type: none"> Resolution: 1 km, monthly, 2001-2020 Data source: 450 m, 8-day, reprocessed MODIS collection 6 LAI (Yuan et al., 2011; Friedl et al., 2019) 	<ul style="list-style-type: none"> Resolution: 0.5°, 12 months Data source: 1 km, 8-day, MODIS collection 4 LAI (Myneni et al., 2002) 	<ul style="list-style-type: none"> Resolution: 0.05°, year 2005 Data source: 450 m, 8-day, reprocessed MODIS collection 5 LAI (Yuan et al., 2011; Friedl et al., 2010)
	Canopy top height, Canopy bottom height	<ul style="list-style-type: none"> Resolution: 1 km, temporally static Data source: 10 m, vegetation canopy height (Lang et al., 2023) 	<ul style="list-style-type: none"> Resolution: 0.5° or PFT specified value, temporally static Tree PFT data source: 1 km, forest canopy height derived using 2005 GLAS aboard ICESat data (Simard et al., 2011); Short vegetation data source: PFT specific values (Bonan et al., 2002) 	--
Soil	Percent sand, Percent clay	<ul style="list-style-type: none"> Resolution: 1 km, temporally static 	<ul style="list-style-type: none"> Resolution: 10 km (0.083°), temporally static 	--
	Soil organic matter	<ul style="list-style-type: none"> Data source: 250 m, Soilgrid v2 (Poggio et al., 2021) 	<ul style="list-style-type: none"> Data source: IGBP soil data of 4931 mapping units (IGBP, 2000) 	--
Topography	Elevation, Slope, Standard deviation of elevation	<ul style="list-style-type: none"> Resolution: 1 km, temporally static Data source: 90 m, MERIT Hydro elevation (Yamazaki et al., 2019) 	<ul style="list-style-type: none"> Resolution: merge of 1 km and 10 arc minutes, temporally static Data source: global most regions are based on USGS HYDRO1k (Verdin and Greenlee 1996); but 10 arc minute data is used over Greenland and Antarctica. 	--
	Aspect, Sky view factor, Terrain configuration factor	<ul style="list-style-type: none"> Resolution: 1 km, temporally static Data source: 90 m, MERIT Hydro elevation (Yamazaki et al., 2019) 	--	--

143 * ELM2 and CLM5 share the same default land surface parameters, detailed descriptions available at:
144 https://escomp.github.io/ctsm-docs/versions/release-clm5.0/html/tech_note/index.html.

147 **2.1 LULC-related parameters**

148 In this study, the MODIS MCD12Q1 version 6 (Friedl et al., 2022) was employed to ascertain the
149 Plant Functional Types (PFT) as well as other non-vegetative land categories at a spatial resolution
150 of 1 km spanning the years 2001 to 2020. The integrity of the MODIS land cover product has been
151 established through a 10-fold cross-validation accuracy assessment using the Terrestrial
152 Ecosystem Parameterization database (Sulla-Menashe et al., 2019). This land cover product offers
153 richer and more flexible land cover data with higher accuracy and substantially less year-to-year
154 stochastic variation in classification results (Sulla-Menashe et al., 2019). Being the sole operational
155 global land cover product available with annual intervals, it addresses a significant gap in the realm
156 of global change research.

157

158 The original MODIS land cover data was first resampled to 1 km from its original 500 m resolution
159 using a majority resampling method in GEE. At such a high 1km resolution, we did not consider
160 the proportion of different land cover types within each grid. Instead, we assigned 100% of a grid
161 cell to the major land cover type. Specifically, the MCD12Q1 LC_Type 5 PFT classification layer
162 was used to determine the distributions of the seven PFTs, as well as lake, urban, and glacier,
163 following the method outlined in Ke et al. (2012) and summarized below:

- 164 • The seven PFTs include needleleaf evergreen trees, needleleaf deciduous trees, broadleaf
165 evergreen trees, broadleaf deciduous trees, shrub, grass, and crop. These PFTs were further
166 reclassified into 15 categories (Table S1) that are typically used in LSMs based on the rules
167 presented in Bonan et al. (2002a) with the assistance of 1 km precipitation and surface air
168 temperature from WorldClim V1 (Hijmans et al., 2005).

- 169 • Grass was reclassified as C3 and C4 grass using the approach presented by Still et al. (2003),
170 with the assistance of monthly LAI (processed in section 2.2.1) and meteorological
171 variables from WorldClim V1.
- 172 • The "non-vegetated land" was classified as barren soil class.
- 173 • The "permanent snow and ice" was assigned as the glacier land unit.
- 174 • Global lakes were identified based on the classification of "water bodies" over the global
175 land, constrained using the global land mask obtained from Natural Earth
176 (<https://www.naturalearthdata.com/>).
- 177 • The urban land unit was determined based on the MODIS "urban and built-up"
178 classification. These urban grids were further classified into three urban classes, namely,
179 tall building district (TBD), high density (HD), and medium density (MD), based on
180 Jackson et al. (2010; hereinafter referred to as J2010). J2010 generated global urban extent
181 maps for the TBD, HD, and MD classes at a spatial resolution of 1 km, based on rules of
182 building height and vegetation coverage fraction
183 (https://gdex.ucar.edu/dataset/188a_oleson/file.html). However, the J2010 dataset is
184 temporally static and cannot reflect changes in urban boundaries over time. Therefore, we
185 reclassified the yearly MODIS urban land class as TBD, HD, and MD based on the J2010
186 dataset using the nearest neighbor sampling method for each year.

187 After determining the distribution of 15 PFTs, bare soil, lake, glacier, and urban land, any
188 remaining 1 km grids were assigned as ocean (Table S1). It should be noted that the wetland land
189 unit was not explicitly classified in this study. This is because, instead of treating wetlands as an
190 individual land unit, many LSMs (e.g., ELM2 and CLM5) integrate wetland functioning processes

191 prognostically within other land units where a surface water storage component is implemented to
192 represent wetland functioning.

193

194 **2.2 Vegetation-related parameters**

195 **2.2.1 Monthly LAI and SAI**

196 The monthly LAI parameters were obtained from Beijing Normal University (BNU_LAI; Yuan et
197 al., 2011). BNU_LAI, an enhanced version of the MODIS LAI product, has been subjected to
198 thorough quality control, incorporating multiple algorithms for improved accuracy (Yuan et al.,
199 2011). Its validation involved an extensive array of LAI reference maps and employed the bottom-
200 up approach advocated by the CEOS Land Product Validation sub-group (Morissette et al., 2006).

201 Compared to the original MODIS LAI, the BNU_LAI dataset exhibits superior performance, along
202 with enhanced spatiotemporal continuity and consistency. The 8-day BNU_LAI product at a
203 resolution of 15 seconds (~450 m) over 2001–2020 was downloaded from
204 <http://globalchange.bnu.edu.cn/research/lai/061>. Subsequently, the data were resampled to a
205 resolution of 1 km using an area-weighted average method and averaged temporally for each
206 month. The processed monthly LAI at 1 km resolution was subsequently assigned to each of the
207 15 PFTs described above at each grid. The monthly SAI was then calculated based on the
208 processed monthly LAI using the methods and PFT parameters described in Zeng et al. (2002).

209

210 **2.2.2 Vegetation canopy height**

211 We leveraged a global vegetation canopy height dataset sourced from Lang et al. (2023). This
212 dataset, derived using a probabilistic deep learning model, fuses Sentinel-2 images with the Global
213 Ecosystem Dynamics Investigation (GEDI) to retrieve canopy height. It stands out as the inaugural

214 global canopy height dataset offering consistent, wall-to-wall coverage at a 10 m spatial resolution
215 across all vegetation types. Assessments using hold-out GEDI reference data and comparisons
216 with independent airborne LiDAR data demonstrate that the approach outlined by Lang et al. (2023)
217 produces a meticulously quality-controlled, state-of-the-art global map product, accompanied by
218 quantitative uncertainty estimates. The canopy height served as the canopy top height parameter.
219 Canopy bottom height was calculated by multiplying PFT-based ratios derived from the ratio of
220 ELM2's (same as CLM5) canopy top and bottom heights for different PFTs (Table S2).

221

222 **2.3 Soil-related parameters**

223 We obtained the Soilgrid v2 data with an original resolution of 250 m (Poggio et al., 2021) to
224 prepare soil properties. Soilgrid is generated using machine learning based on multiple data
225 sources of soil profiles and remote sensing data (Hengl et al., 2017). The soil product underwent
226 rigorous quantitative evaluation using a cross-validation method, which ensures alignment with
227 established pedo-landscape features and provides spatial uncertainty to guide product users
228 (Poggio et al., 2021). Soilgrid v2 provides percent clay, percent sand, and soil organic matter for
229 six standard soil layers: 0–5 cm, 5–15 cm, 15–30 cm, 30–60 cm, 60–100 cm, and 100–200 cm.
230 The original SoilGrid version 2 data obtained from GEE were processed at 1 km resolution with
231 multiple layers using an area-weighted average method. To facilitate the demonstration, we
232 restructured the six soil layers vertically into ELM2's ten effective soil layers (0–1.8 cm, 1.8–4.5
233 cm, 4.5–9.1 cm, 9.1–16.6 cm, 16.6–28.9 cm, 28.9–49.3 cm, 49.3–82.9 cm, 82.9–138.3 cm, 138.3–
234 229.6 cm, and 229.6–380.2 cm) using the nearest neighboring method. It should be noted that the
235 lake module in ELM2 and CLM5 requires soil properties, but the Soilgrid v2 data may not provide

236 coverage over water surfaces. To address this, we utilized the nearest neighbor sampling method
237 to map the 1 km soil properties onto the terrestrial water surface.

238

239 **2.4 Topography-related parameters**

240 We employed the digital elevation from the Multi-Error-Removed Improved-Terrain DEM
241 (MERIT DEM, Yamazaki et al., 2019) to obtain topography-related parameters. The MERIT DEM
242 provides globally consistent elevation data at 90 m resolution, distinguished by its exceptional
243 vertical accuracy. This accuracy was rigorously validated against ICESat’s lowest elevations in
244 both forested and non-forested regions and was further benchmarked using the UK’s premium
245 airborne LiDAR DEM (Yamazaki et al., 2019). We first acquired the 1km elevation and standard
246 deviation of elevation using GEE based on the original 90 m elevation. Further, we calculated the
247 slope, aspect, sky view factor, and terrain configuration factor from the 1km elevation using the
248 parallel computing tool developed by Dozier (2022). The sky view factor represents the proportion
249 of visible sky limited by adjacent terrain, and the terrain configuration factor describes the
250 proportion of adjacent terrain which is visible to the ground target. Finally, to drive the
251 parameterization of sub-grid topographical effects on solar radiation (Hao et al., 2022) in ELM2,
252 we calculated the $\sin(\text{slope}) \cdot \sin(\text{aspect})$ and $\sin(\text{slope}) \cdot \cos(\text{aspect})$ for calculating the
253 local solar incident angle, and two normalized angle-related factors, the sky view factor, and terrain
254 configuration factor by $\cos(\text{slope})$. It is important to note that the standard deviation of elevation
255 calculated in this study is specific to the 1 km resolution simulation. For applications requiring
256 coarser resolutions (e.g., 0.5 degree), the standard deviation should be recalculated directly from
257 the 1 km elevation, rather than averaging from the 1k standard deviation of elevation.

258

259 **2.5 Comparison between new and existing land surface parameters**

260 In this study, since the data sources used to develop the 1k global land surface parameters have
261 already undergone rigorous validation, we do not perform additional evaluations against reference
262 datasets (e.g., observations). Instead, our focus is on comparing the newly developed 1k
263 parameters with those from K2012 and the ELM2/CLM5 default parameters. The K2012
264 parameters, obtained through personal communication (refer to the data availability section for
265 details). The ELM2/CLM5 default parameters were sourced from the CESM input data repository
266 (<https://svn-ccsm-inputdata.cgd.ucar.edu/trunk/inputdata/>). Given the different resolutions of
267 these datasets—our new parameters at 1km, K2012 at 0.05 degree, and ELM2/CLM5 defaults with
268 varying resolutions—we adapt our comparison at different resolutions for different variables.

269 For PFT parameters, we aggregated both the 1k new parameters and the 0.05-degree K2012 data
270 to the 0.5-degree resolution of the ELM2/CLM5 default. For non-vegetated land units (i.e., urban,
271 glacier, and lake), we upscaled the 1k new parameters to a 0.05-degree resolution to align with the
272 ELM2/CLM5 default. It is important to note that the urban parameter in K2012 is only available
273 for the northern hemisphere, due to limitations in data acquisition.

274 When comparing LAI, we aggregated the 1k new and K2012 LAI to 0.5-degree resolution,
275 matching the ELM2/CLM5 default LAI/SAI resolution. We excluded the comparison of SAI from
276 our analysis due to the limited availability of the global K2012 dataset, from which we only
277 acquired coverage for North America. We have not included a comparison of vegetation canopy
278 height (top and bottom parameters) in our study. This is because the K2012 dataset does not
279 contain these parameters, and the ELM2/CLM5 default parameters in the CESM input data
280 repository provide only tabular values for each PFT, rather than spatially variable canopy heights
281 for tree PFTs.

282 For soil and topography-related parameters, our comparison was limited to the 1k new parameters
283 and the ELM2/CLM5 default, as K2012 does not include these parameters. Specifically, for soil
284 comparisons, we aggregated the new 1k parameters to 0.083° resolution to match the ELM2/CLM5
285 default soil parameters. For topography, given that the ELM2/CLM5 default parameters is a
286 combination of 1k and 10 arc-minute data sources, we simplify the comparison by aggregating
287 both the new 1k parameters and ELM2/CLM5 default to 0.5-degree resolution, including elevation
288 and slope.
289

290 **3. K-scale demonstration simulation over CONUS**

291 **3.1 Experiment design**

292 To demonstrate the capability of 1 km datasets, we conducted ELM2 simulations over CONUS at
293 the resolution of 1 km, using the newly developed 1 km land surface parameters for 2010. We used
294 atmospheric forcing from the Global Soil Wetness Project Phase 3 (GSWP3; Kim, 2017) with a
295 spatial resolution of 0.5° to drive ELM. The spatial homogeneity of atmospheric forcings within
296 0.5° grid cell guarantees that the spatial variability of ELM simulated variables (e.g., latent heat)
297 within 0.5° grid cell is solely attributable to the heterogeneity of the 1 km land surface parameters.
298 There are approximately 12 million effective grids over CONUS. We ran ELM for five years
299 (2010–2014), and the last year’s simulation was used for analysis. We specifically analyzed the
300 annual mean of surface layer soil moisture (SM, m^3/m^3), latent heat (LH, W/m^2), emitted
301 longwave radiation (ELR, W/m^2), and absorbed shortwave radiation (ASR, W/m^2).

302 **3.2 Spatial scaling analysis**

303 We conducted a spatial scaling analysis following the method described in Vergopolan (2022) on
304 the 1 km ELM simulation data to better understand how k-scale spatial heterogeneity in the four
305 ELM-simulated variables (mentioned in Section 3.1) induced only by spatial heterogeneity of land
306 surface parameters changes across spatial scales. First, we performed upscaling by averaging the
307 1 km ($=1/120^\circ$) land surface parameters and the four ELM-simulated variables to coarser spatial
308 scales, λ_{scale} of $1/60^\circ$, $1/40^\circ$, $1/30^\circ$, $1/24^\circ$, $1/20^\circ$, and $1/10^\circ$, and calculated the spatial standard
309 deviation (σ_{scale}) within each $0.5^\circ \times 0.5^\circ$ box at each spatial scale (Table 2). Second, we quantified
310 the changes in spatial variability at different spatial scales compared to the original 1km resolution
311 by calculating the ratio of σ_{scale} to $\sigma_{1 km}$. Third, we fitted a $\log\left(\frac{\sigma_{scale}}{\sigma_{1 km}}\right) \propto \beta \times \log\left(\frac{\lambda_{scale}}{\lambda_{1 km}}\right)$
312 relationship, where β is an indicator to quantify data spatial variability persistence across scales

313 (Hu et al., 1997). A more negative β indicates a larger dependency of data spatial variability on
 314 spatial scales, resulting in a higher information loss, denoted as $\gamma_{scale} = (1 - \sigma_{scale}/\sigma_{1\text{ km}}) \times$
 315 100%. In this study, we focus on information loss at a 12 km scale, denoted as $\gamma_{12\text{ km}}$. For
 316 simplicity in subsequent discussion, $\gamma_{12\text{ km}}$ will be referred to as γ in the results section. Given the
 317 possibility that β may not demonstrate significant temporal variation (Mälicke et al., 2020), and
 318 considering that our scaling analysis is intended for demonstration purposes, our spatial scaling
 319 analysis is based on the annual mean of ELM2 simulations.

320 Table 2. Spatial resolution and pixel number at different spatial scales.

$\lambda_{scale}/\lambda_{1\text{ km}}$	1	2	3	4	5	6	12
Spatial resolution	1km (1/120°)	2km (1/60°)	3km (1/40°)	4km (1/30°)	5km (1/24°)	6km (1/20°)	12km (1/10°)
Pixel number within 0.5° × 0.5° box	60 × 60	30 × 30	20 × 20	15 × 15	12 × 12	10 × 10	5 × 5

321

322 **3.3 Attribution analysis utilizing XML methods**

323 We conducted additional analysis to determine the primary land surface parameters that influence
 324 the spatial scaling of ELM simulations. We employed XML methods, specifically the eXtreme
 325 Gradient Boosting(XGBoost; Chen and Guestrin, 2016) machine learning algorithm and the game
 326 theoretic approach SHapley Additive exPlanations (SHAP; Lundberg and Lee, 2017; Lundberg et
 327 al., 2018, 2020). XML methods were utilized to assess the influence of land surface parameters on
 328 the spatial variability and information loss of ELM2 simulations across the CONUS. Taking spatial
 329 variability as an example, we first computed the standard deviation (σ) within each 0.5° x 0.5° grid
 330 for both 1 km resolution land surface parameters and simulations. Then, we train a machine
 331 learning model to predict the spatial variability of each simulated variable (i.e., SM, LH, ELR,
 332 ASR). We used the spatial variability (i.e., σ) and mean (μ) of the land surface parameters and μ

333 of precipitation and temperature as predictor variables, and the simulated variable's σ as the target
334 variable. After training the machine learning model, we used SHAP to quantify the relative
335 importance and determine which factors were most important in driving the spatial variability of
336 the simulations. Similarly, we used this approach to identify the most critical drivers of information
337 loss.

338

339 **3. Results**

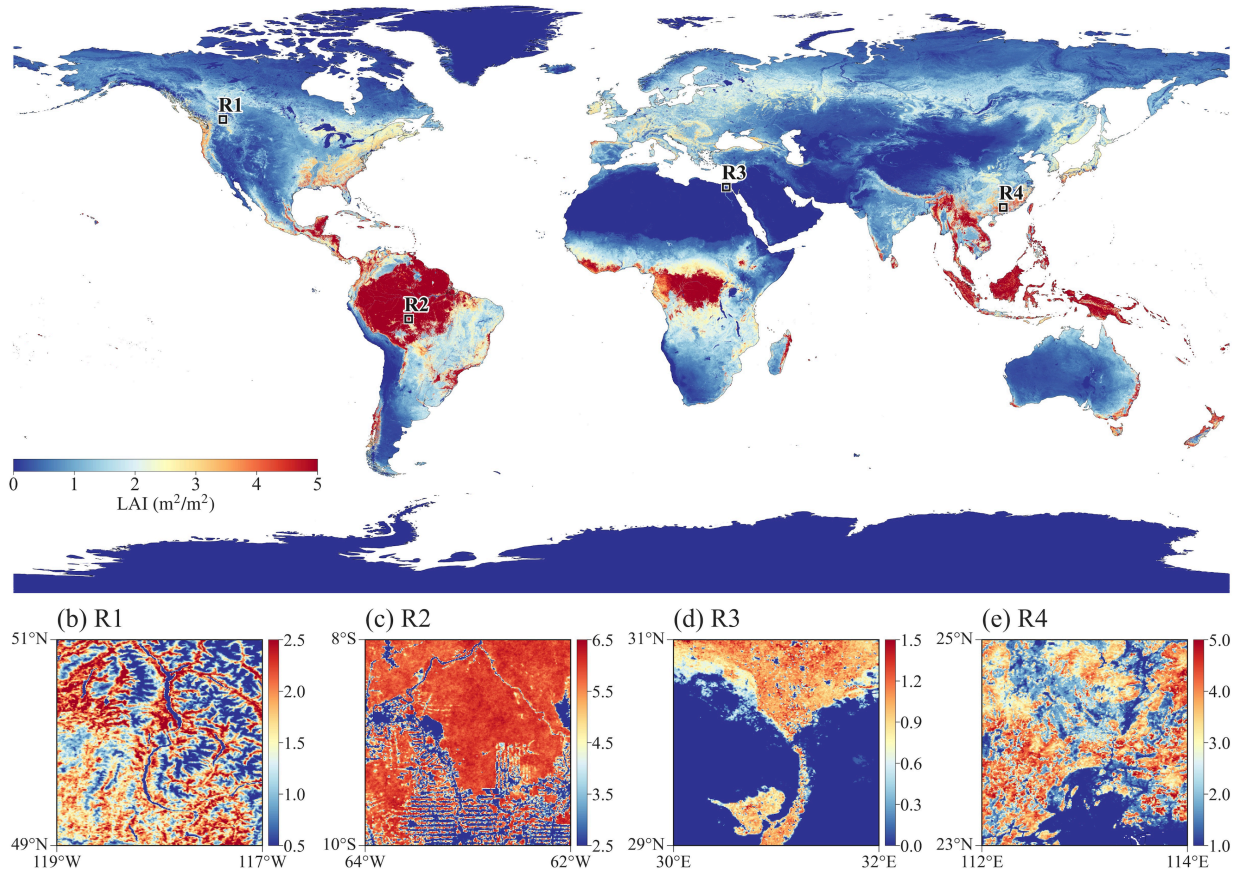
340 **3.1 Demonstration of the global 1km land surface parameters**

341 LAI generally shows high values in humid and warm regions, such as tropical rainforests,
342 southeastern US, and southern Asia, and low values over arid or cold regions, such as central
343 Australia, southwestern US, Middle East, Central Asia, and northern Canada (Figure 1a). At high
344 resolution, the LAI dataset clearly reflects the detailed heterogeneity of vegetation distributions.
345 In subregion R1 (Figure 1b), a relatively small LAI is distributed over mountain ridges and zero
346 LAI over water surfaces (e.g., lakes). In subregion R2 (Figure 1c), the LAI pattern shows a large
347 proportion of forest fragmentation caused by deforestation. In subregion R3 (Figure 1d), the LAI
348 shows the distribution of agricultural land along with the river, river mouth, and lakes under an
349 arid climate. R4 shows how urbanization affects vegetation distributions (Figure 1e).

350 Figure 2 demonstrates the distribution of plant functional types and other non-vegetation land units.
351 High-resolution LULC types over multiple years can benefit studies related to LULC changes like
352 urbanization and deforestation. Canopy height generally follows a similar spatial pattern with LAI,
353 with high values in humid and warm regions and low values over arid or cold regions (Figure 3a).
354 The percent clay shows high values over Southeast Asia, India, central Africa, and southeast South
355 America, and low content over North Europe, South Africa and Alaska (Figure 3b). The

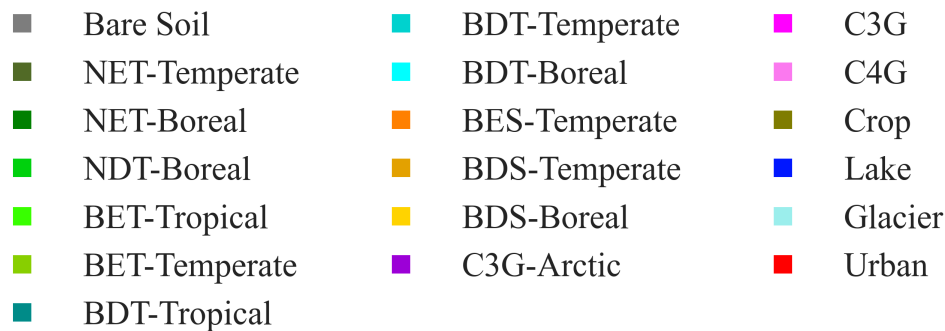
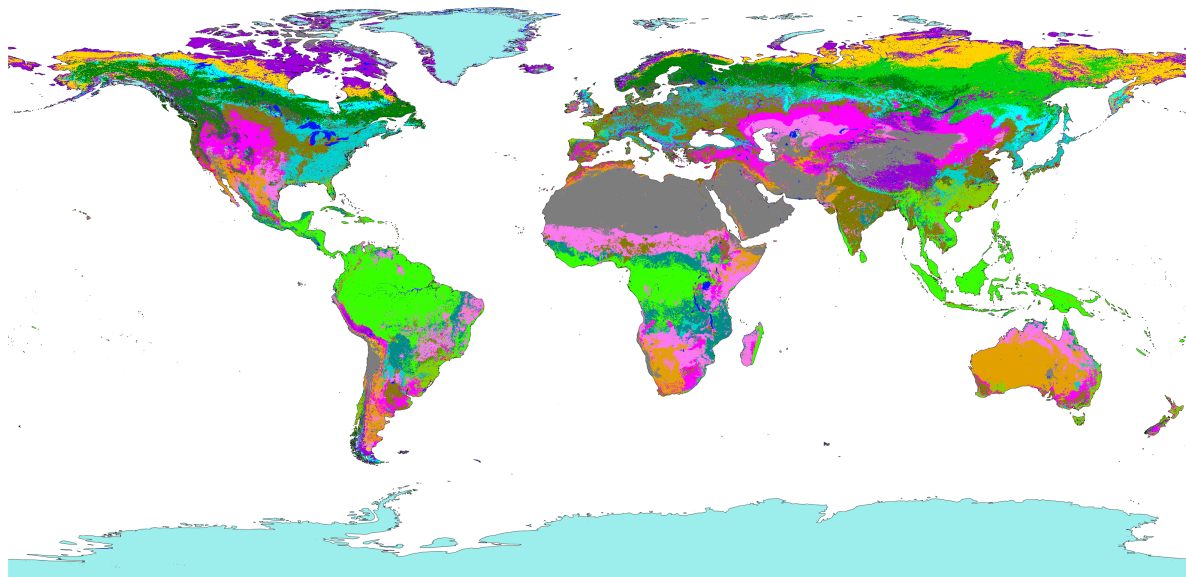
356 topography factors follow the elevation patterns (Figures 3c and 3d), where there are large slopes
357 and standard deviation of elevation over mountainous regions, such as the Rocky Mountains in
358 North America, the Himalayas Mountains in Asia, and Andes Mountains in South America.

(a) LAI (m^2/m^2)



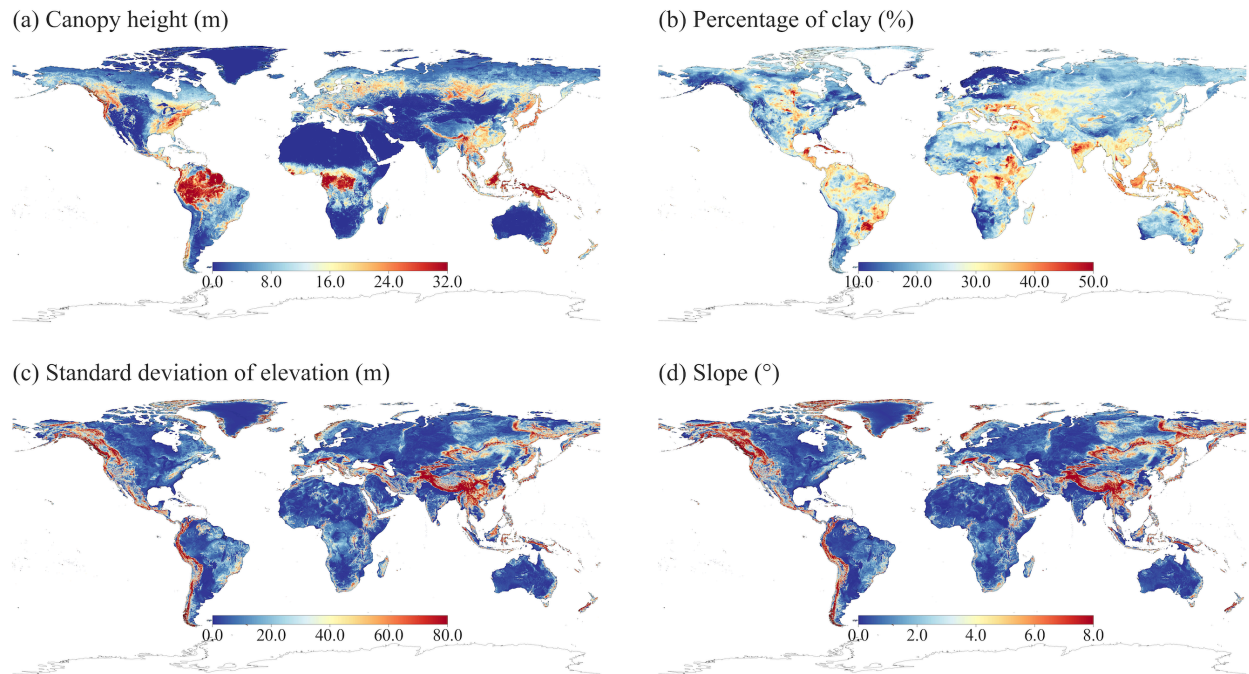
359
360 Figure 1. The spatial pattern of LAI (annual mean in 2010) over (a) global land and (b)~(e) four
361 subregions R1~R4 within 2-degree boxes marked in (a). Subregions R1~R4 represent
362 topography, deforestation, irrigations, and urbanization effects on LAI.

363



364

365 Figure 2. Global LULC distribution in year 2010. PFT abbreviations include: Bare Soil, Needleleaf
 366 Evergreen Trees in temperate (NET-Temperate) and boreal (NET-Boreal) regions, Needleleaf
 367 Deciduous Trees in boreal regions (NDT-Boreal), Broadleaf Evergreen Trees in tropical (BET-
 368 Tropical) and temperate (BET-Temperate) regions, Broadleaf Deciduous Trees in tropical (BDT-
 369 Tropical), temperate (BDT-Temperate), and boreal (BDT-Boreal) regions, Broadleaf Evergreen
 370 Shrubs in temperate regions (BES-Temperate), Deciduous Shrubs in temperate (BDS-Temperate)
 371 and boreal (BDS-Boreal) regions, C3 Grass in arctic (C3G-Arctic) and general (C3G) varieties,
 372 C4 Grass (C4G), Crop, Lake, Glacier, and Urban.



373

374 Figure 3. Demonstration of global 1km datasets (a) Canopy top height, (b) percent clay, (c)

375

standard deviation of elevation, and (d) slope.

376

377 3.2 Comparison between new and existing land surface parameters

378 The global distributions of different PFTs show varying degrees of difference when comparing the

379 new parameters with the K2012 and ELM2/CLM5 default parameters (Figure 4 and

380 Supplementary Figures S1 to S16). Predominant types such as bare soil, BET-Tropical tree, C3

381 and C4 grass, and crop are found consistently across all datasets. Notable differences include less

382 bare soil in the new parameters and K2012 compared to ELM2/CLM5 default, especially in high-

383 latitude North America, western US, South Africa, Central Asia, and Central Australia (Figure S1).

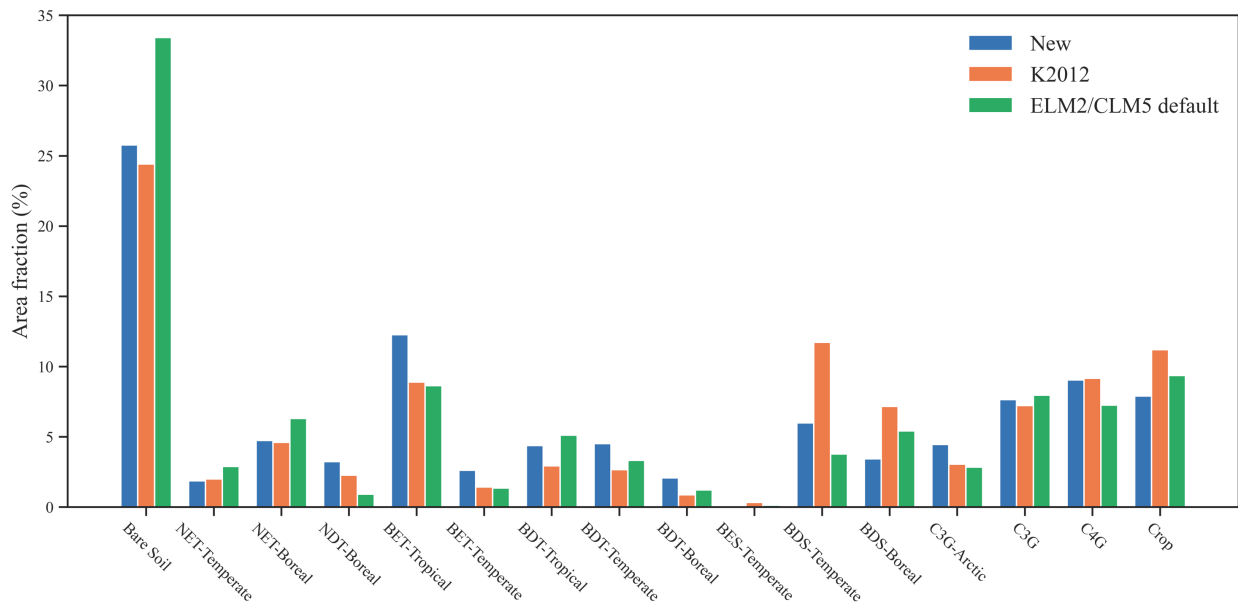
384 While the new NDT PFT shows larger coverage in Siberia than K2012 and ELM2/CLM5 (Figure

385 S4), BET-Tropical PFT is more prevalent in the new parameters across Central and South America

386 (Figure S5). BET-Temperate PFT has greater area coverage in southern China in the new

387 parameters (Figure S6). For BDT-Tropical, BDT-Temperate, and BDT-Boreal PFTs, both the new

388 and ELM2/CLM5 default parameters surpass K2012 data in coverage (Figures S7 to S9). The
 389 coverage of new BDS-Temperate PFT is smaller than K2012 but larger than ELM2/CLM5 default
 390 (Figure S11), and the new BDS-Boreal PFT is less extensive in the boreal northern hemisphere
 391 compared to both K2012 and ELM2/CLM5 defaults (Figure S12). The C3-Arctic PFT shows
 392 larger areas in the new parameters, particularly in northern Canada, with the new C4 grass PFT
 393 being similar to that of K2012 and larger than ELM2/CLM5 C4 grass. Crop PFT is less extensive
 394 in the new parameters, particularly in Southeastern China, Europe, South America, Africa, and
 395 Australia.



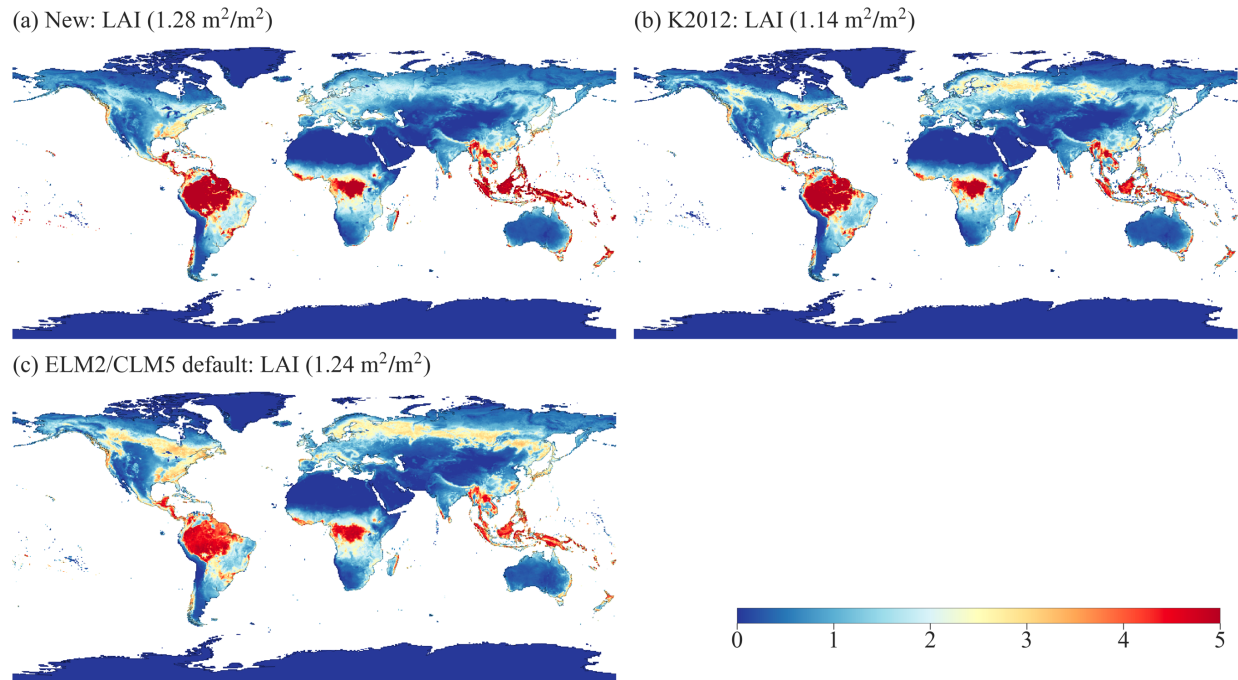
396
 397 Figure 4. The global average area fractions of PFTs for three land surface parameter datasets. PFT
 398 abbreviations used on the X-axis are displayed in Figure 2.

399
 400 The global distributions of non-vegetated land covers of lake, glacier and urban areas vary among
 401 the datasets (Figure S17–S19). The new dataset shows slightly less lake coverage than K2012, but
 402 both are smaller than ELM2/CLM5 default, particularly in high-latitude North America (Figure
 403 S17). Glacier coverage in the new parameter is around 0.7% smaller than K2012, with noticeable

404 differences in the Arctic North America, while ELM2/CLM5 default shows more extensive glacier
405 coverage in Antarctica (Figure S18). Regarding urban areas, K2012 has the smallest urban
406 coverage in the Northern Hemisphere compared to both the new dataset and ELM2/CLM5 default
407 (Figure S19). Meanwhile, ELM2/CLM5 default exhibits more expansive urban areas in India and
408 China than the new dataset and K2012.

409

410 The global annual mean LAI exhibits similar spatial patterns among the new parameter, K2012,
411 and ELM2/CLM5 (Figure 5). The overall global mean LAI for the new parameter ($1.28 \text{ m}^2/\text{m}^2$) is
412 slightly higher than that of K2012 ($1.14 \text{ m}^2/\text{m}^2$) and the ELM2/CLM5 default data ($1.24 \text{ m}^2/\text{m}^2$).
413 In terms of spatial pattern, the new LAI, relative to K2012 (Figure S20a), shows lower values in
414 the NET-Boreal PFT over the northern hemisphere, but higher values in the BET-Tropical PFT
415 over the tropics. Similarly, compared with the ELM2/CLM5 default LAI (Figure S20b), the new
416 LAI also presents smaller values in both the NET-Boreal and NDT PFTs over the northern
417 hemisphere, but larger values in the BET-Tropical PFT regions.



418

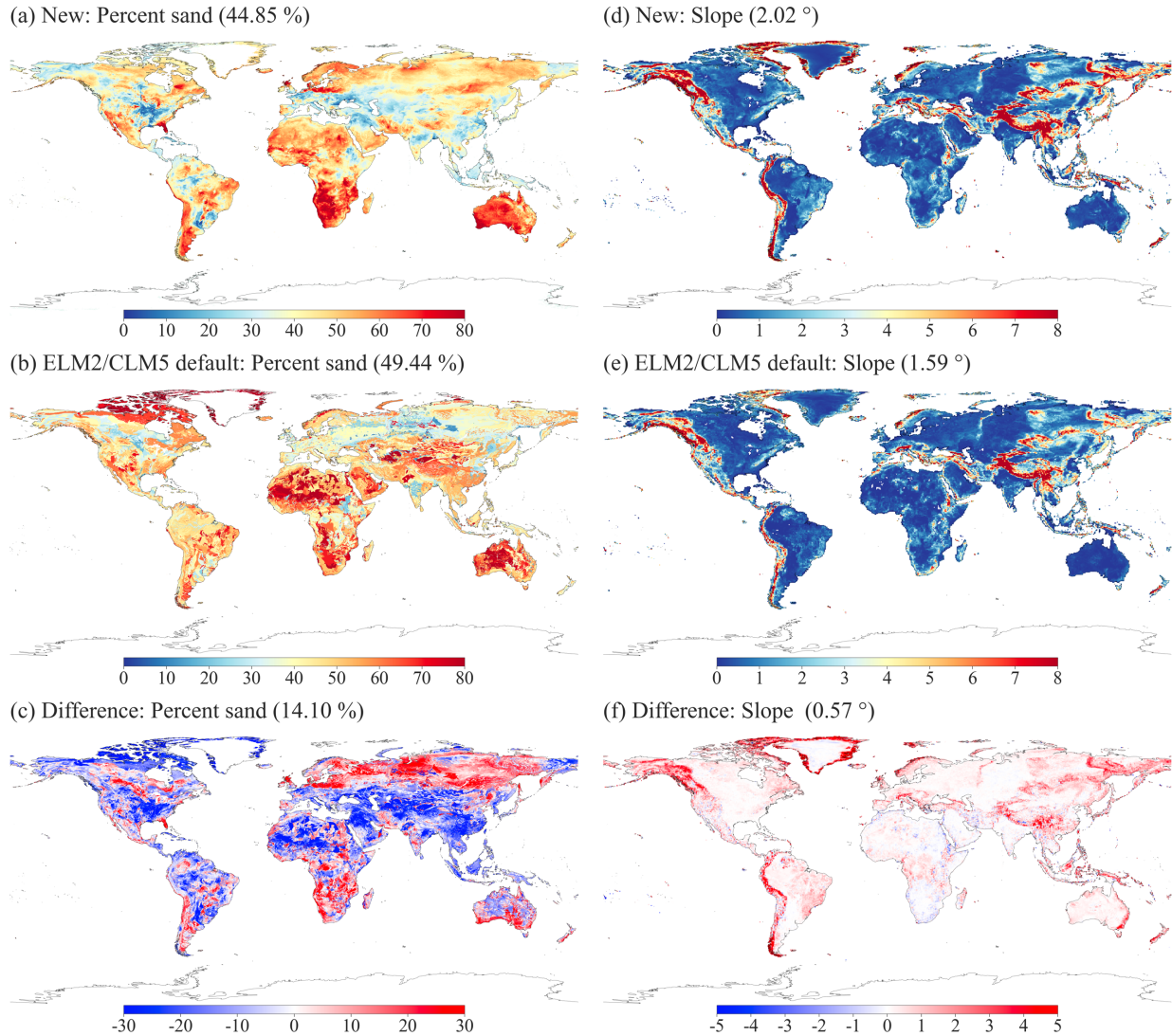
419 Figure 5. Comparison of global annual mean LAI for (a) new, (b) K2012, and (c) ELM2/CLM5
 420 default parameters. The global average is indicated in the subplot title.

421

422 Soil parameters exhibit significant differences between the new and ELM2/CLM5 default datasets
 423 (Figures 6a-bc, S21, and S22). The global mean absolute differences between the new and
 424 ELM2/CLM5 default for percent sand, percent clay, and organic matter are 14.1%, 8.1%, and 30.5
 425 kg/m³, respectively. Generally, the new soil parameters are spatially distributed more smoothly
 426 than those from ELM2/CLM5 with more patchy patterns (Figure 6a vs. 6b). Specifically, the new
 427 percent sand is higher in regions like Europe, Siberia, South Africa, and Southern Australia, but
 428 lower in areas such as the Lower Mississippi River Basin, North Africa, and Central and
 429 Southeastern Asia (Figure 6c). The new percent clay shows larger values in the Western US, North
 430 Africa, Central Asia, and Australia, but smaller values in Alaska and Eastern Europe (Figure S21).

431 For organic matter, the new parameter indicates smaller values in the Northern Hemisphere but
432 larger values in other global regions compared to the ELM2/CLM5 default (Figure S22).

433 Topography-related parameters exhibit broadly similar spatial patterns but with notable
434 differences between the new and ELM2/CLM5 default parameters, as seen in Figures 6d-6f and
435 S23. The new slope parameter generally shows a larger slope relative to the ELM2/CLM5 default,
436 particularly in mountainous regions (Figure 6f). This could be attributed to the new 1 km slope
437 being calculated from a finer 90 m resolution elevation. Differences in elevation between the new
438 and ELM2/CLM5 parameters are more pronounced in areas such as various mountainous regions,
439 Greenland, the Amazon Basin, the Tibetan Plateau, and Australia (Figure S23).



440

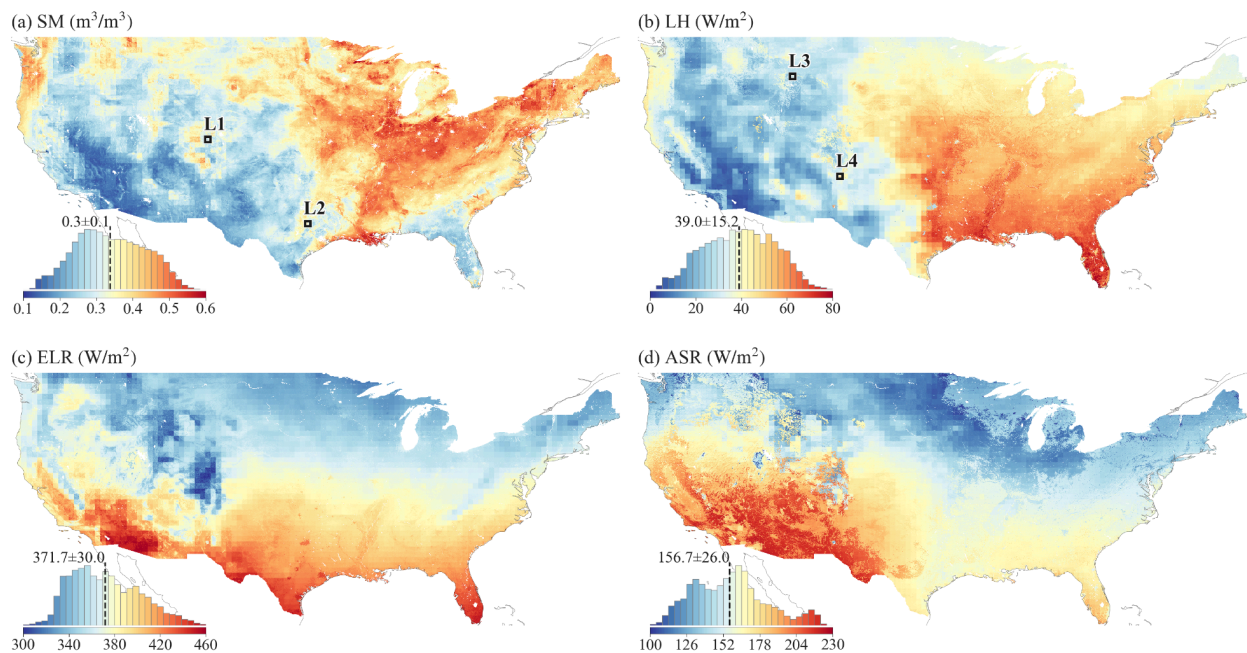
441 Figure 6. Comparisons of percent sand and slope. (a) new and (b) ELM2/CLM5 default percent
 442 sand, along with (c) their difference (new – ELM2/CLM5 default) for percent sand; (d) new, (e)
 443 ELM2/CLM5 default, and (f) their difference for slope. The global average is shown in the subplot
 444 titles, with the global average of the absolute difference provided for (c) and (f).

445

446 3.3 Demonstration 1km simulation over CONUS

447 ELM simulations at a 1 km resolution display significant spatial heterogeneity over CONUS
 448 (Figure 7). The values of SM, LH, ELR, and ASR across CONUS follow approximately normal

449 distributions, with averages of $0.3 \text{ m}^3/\text{m}^3$, $39.0 \text{ W}/\text{m}^2$, $371.7 \text{ W}/\text{m}^2$, $156.7 \text{ W}/\text{m}^2$, respectively (as
 450 shown in the histogram plots in Figure 7). SM shows drier conditions over the West and Southwest
 451 and wetter conditions over the Midwest, Corn Belt, Mississippi River basin, and Northeast (Figure
 452 7a). LH shows high values over the central and southeast, and lower values over the west and
 453 southwest (Figure 7b). The ELR generally shows higher values over regions with high surface
 454 temperature in the south (Figure 7c). The ASR shows higher values over the southwestern regions
 455 determined by incoming solar radiation and albedo (Figure 7d). Despite the high-resolution
 456 heterogeneity shown at 1 km resolution, we can still see the spatial patterns distinguished at coarse
 457 resolution, i.e., $0.5^\circ \times 0.5^\circ$. These coarser footprints are from the GSWP3 atmospheric forcing with
 458 0.5° resolution. As concluded by Li et al. (2022), atmospheric forcing is one primary heterogeneity
 459 source for land surface modeling. Therefore, k-scale atmospheric forcing needs to be developed to
 460 further advance k-scale offline land surface modeling.



461
 462 Figure 7. The annual mean of 1 km simulations of (a) SM, (b) LH, (c) ELR, and (ASR) over
 463 CONUS. The $0.5^\circ \times 0.5^\circ$ boxes marked as L1, L2, L3, and L4 in (a) and (b) are selected to

464 demonstrate the spatial scaling analysis. The inserted histogram plot illustrates the distribution of
465 ELM2 simulations.

466

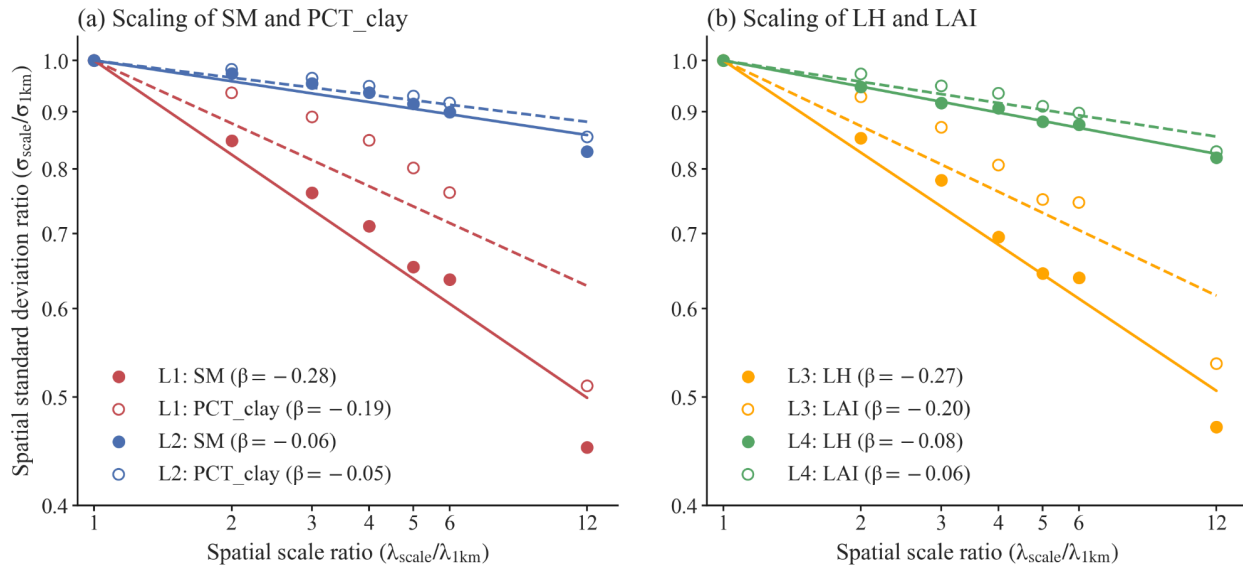
467 **3.4 Demonstration of spatial scaling across scales**

468 We next demonstrate the relationships between spatial variabilities and spatial scales for SM and
469 LH. Four locations (in Figures 4a and 4b) are specifically chosen to showcase varying levels of
470 spatial information loss: L1 and L3 demonstrate a relatively large loss for SM and LH, respectively,
471 while L2 and L4 represent a relatively small loss for SM and LH, respectively.

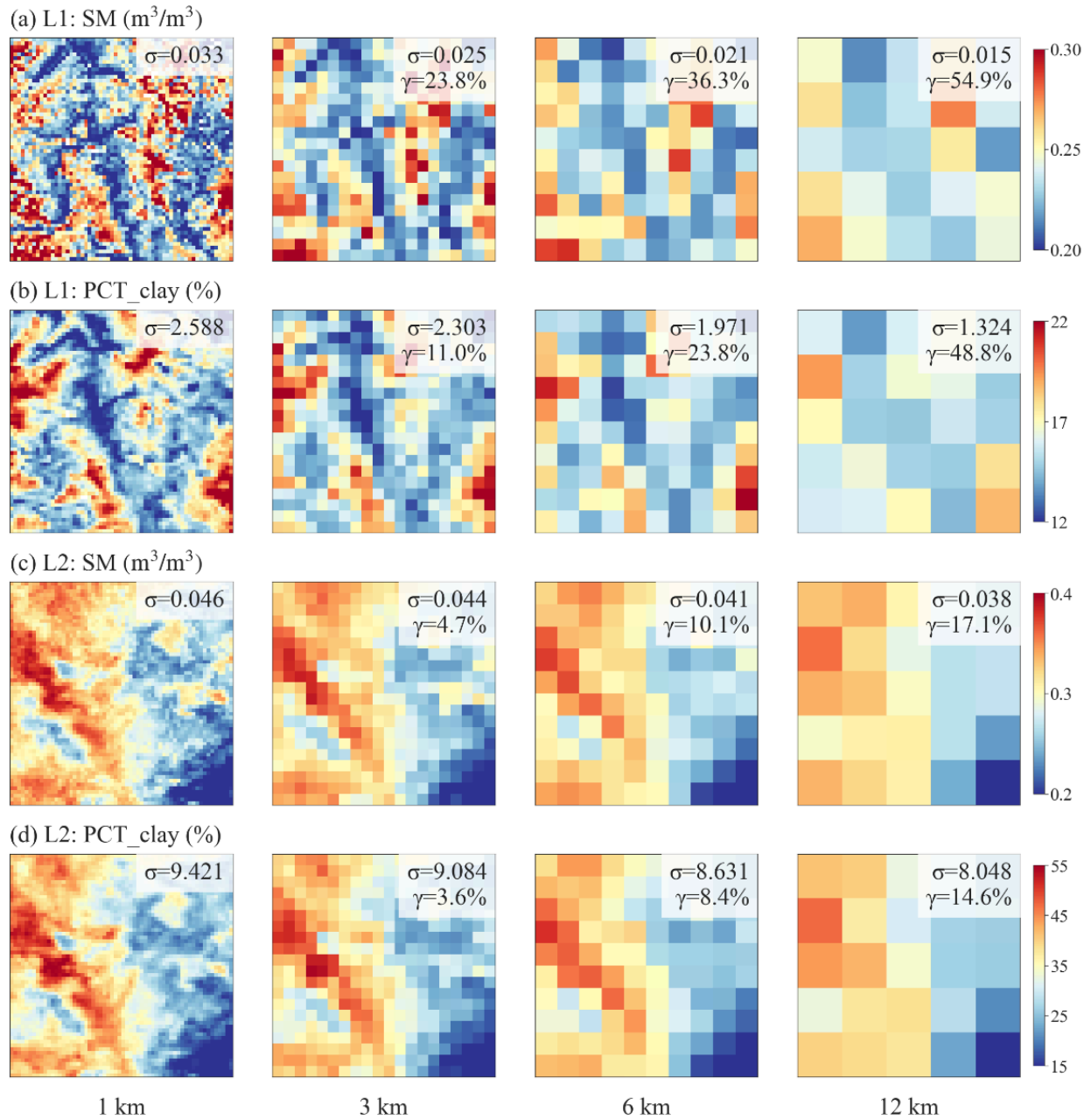
472 At location L1 (Figure 8a), when the 1 km simulation is upscaled to coarser resolutions (i.e., larger
473 spatial scale ratios), the spatial variability of SM decreases, resulting in a negative slope of β . As
474 shown in Figure 9a, compared to the original 1 km resolution, the information loss γ reaches up to
475 54.9% at the 12 km spatial scale. The spatial pattern of SM is consistent with the spatial pattern of
476 percent clay (Figures 6a vs. 6b and 6c vs. 6d), indicating that soil texture contributes significantly
477 to the spatial variability of SM. However, SM has a more negative β than the percent clay ($\beta = -$
478 0.28 vs. -0.19 at L1, as shown in Figure 8a), suggesting that SM variability is amplified likely by
479 other processes that are also influenced by soil texture. In contrast to location L1, location L2
480 exhibits less negative β values for both SM and percent clay, suggesting that their spatial
481 variabilities exhibit less scale dependence (Figures 5a, 6c, and 6d). Both SM and percent clay at
482 location L2 approximately maintain their spatial patterns of high values in the west and low values
483 in the east across spatial scales (Figures 6c and 6d).

484 For LH, there is a more negative β value at location L3 than at location L4 ($\beta = -0.27$ at L3 vs. $-$
485 0.08 at L4, as shown in Figure 8b), which indicates a larger decrease of spatial variability across
486 spatial scales and lower variability persistence at location L3 than location L4 (Figure 10). The

487 spatial pattern of LH is consistent with the spatial pattern of LAI (Figures 7a vs. 7b and 7c vs. 7d)
 488 at different spatial scales, suggesting that vegetation plays a significant role in the spatial
 489 variability of LH. Similar to comparison between SM and soil texture, LH has a more negative β
 490 than LAI (Figure 8b).



491
 492 Figure 8. The scaling of spatial variabilities for (a) SM and percent clay, and (b) LH and LAI. Both
 493 the x-axis and y-axis are in logarithmic scale. The slope of the linear regression line, β , quantifies
 494 the strength of the negative relationship between spatial scale and spatial variability. A more
 495 negative β value indicates a higher spatial-scale dependency and increased information loss at
 496 coarser spatial scales. Four $0.5^\circ \times 0.5^\circ$ boxes (displayed in Figure 7), namely L1 to L4, are chosen
 497 to contrast larger and smaller negative β values for SM and percent clay (L1 and L2) and for LH
 498 and LAI (L3 and L4).

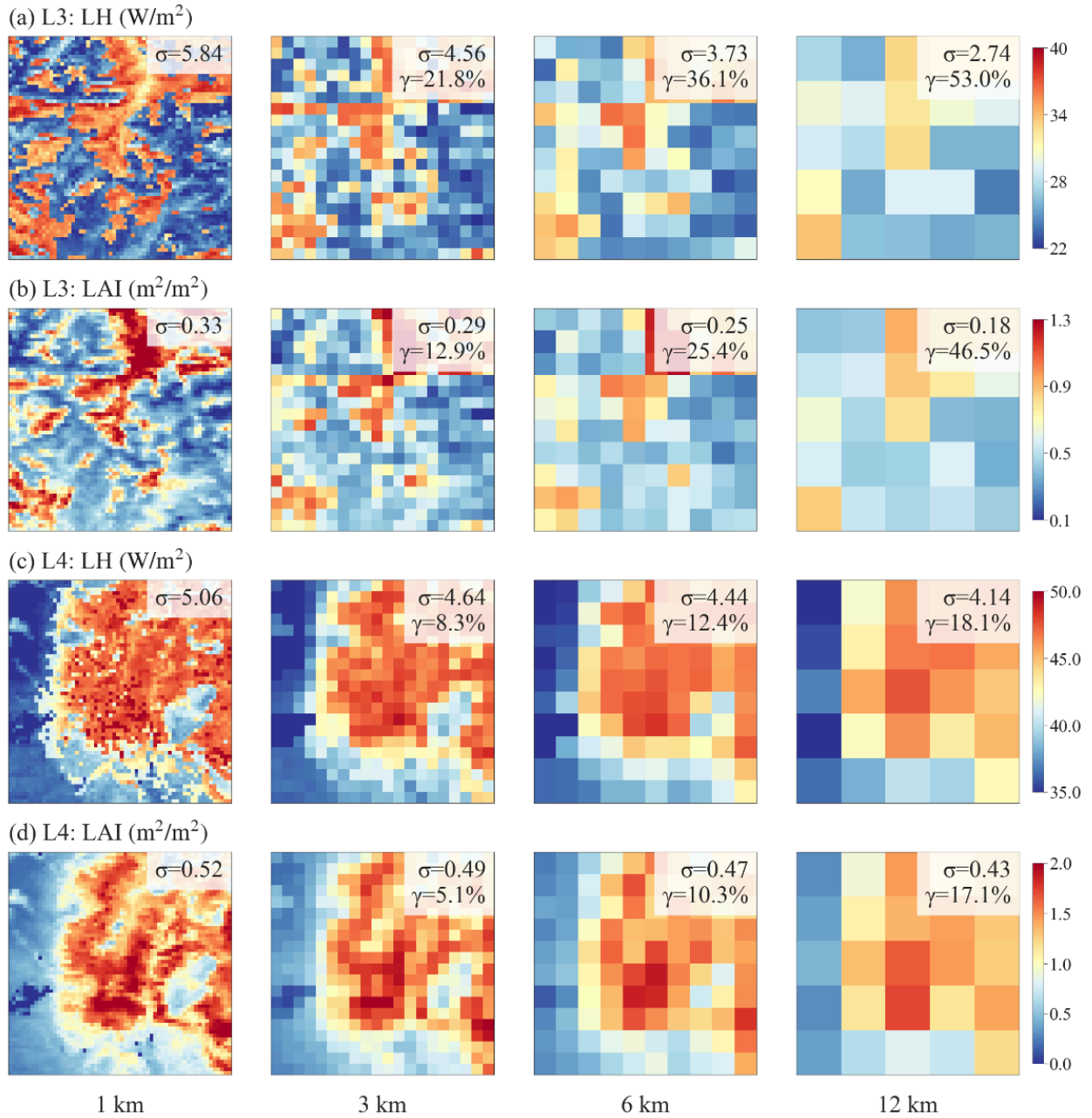


499

500 Figure 9. Comparison of SM and percent clay across spatial scales at locations L1 and L2

501 highlighted in Figure 7. Each subplot displays the spatial patterns of SM or percent clay within a

502 $0.5^\circ \times 0.5^\circ$ box, with the σ and γ presented in the legend.



503

504 Figure 10. Similar to Figure 9, but for LH and LAI at locations L3 and L4.

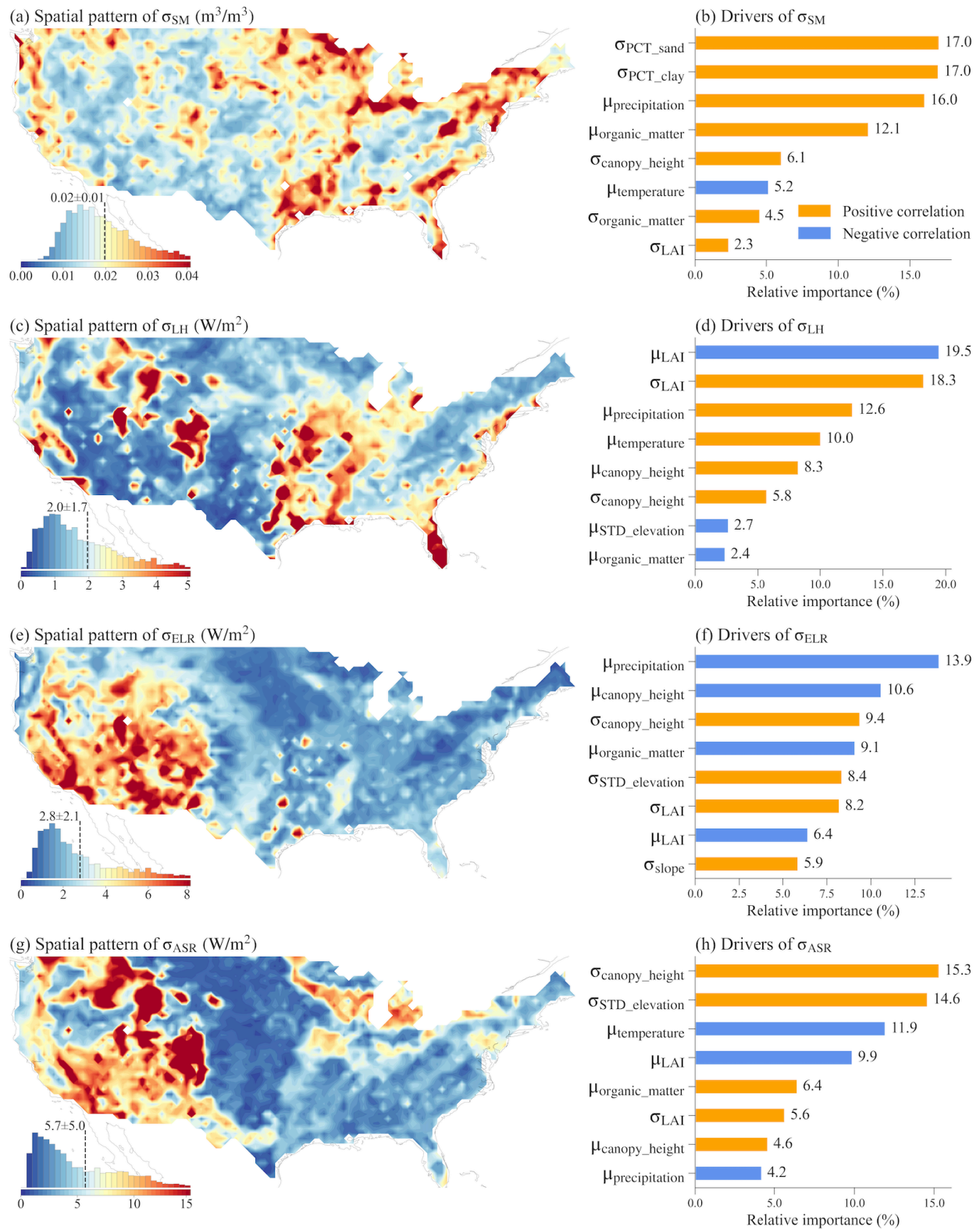
505 3.5 The spatial variability of water and energy simulations and their drivers

506 We quantified the spatial variability simulated at 1 km resolution using σ within each $0.5^\circ \times 0.5^\circ$
507 box across CONUS. Four ML models were built to explore the spatial relationships between σ and
508 its potential drivers including σ of the land surface parameters and the temperature and
509 precipitation averaged over the grid box. Overall, the ML models performed well in predicting the
510 σ of the simulated variables, with small root mean square error (RMSE) and large R^2 (see Figure
511 S24). SM shows larger spatial variability in the US Southern Coastal Plain, lower Mississippi
512 River, Northeast, Southeast, and regions around the Great Lake (Figure 11a), which is roughly
513 consistent with the spatial heterogeneity of the high-resolution SM simulation in Vergopolan et al.
514 (2022). Based on the SHAP method, the spatial variability of SM across CONUS is driven by
515 various factors, mainly including the spatial variabilities of percent sand and percent clay, mean
516 precipitation, the σ and μ of soil organic matter, the σ of canopy height, and mean temperature
517 (Figure 11b). Mean precipitation and temperature reflect climate conditions (Figure S26), which
518 are related to the water supply and water demand of soil water content. The spatial heterogeneity
519 of soil properties, such as texture and organic matter content, affects soil hydraulic properties and
520 generate more spatially variable soil water content. Vegetation characteristics, such as canopy
521 height and LAI, could influence SM spatial variability through their effect on roughness length
522 and rooting depth.

523 The spatial variability of LH is large in the southeastern, central, and western mountainous regions
524 of the US (Figure 11c). Vegetation properties and climate conditions mainly drive the variability
525 of LH (Figure 11d). The μ and σ of LAI can affect transpiration and soil evaporation, while canopy
526 height can influence surface roughness length and, in turn, evapotranspiration. Mean precipitation

527 and temperature reflect the overall climate conditions related to the water and energy available for
528 latent heat.

529 ELR and ASR exhibit large spatial variability mainly over the western US, with ASR additionally
530 showing significant spatial variability across the Northern US (Figures 8e and 8g). This variability
531 is primarily driven by climate conditions such as mean precipitation and temperature, topographic
532 features such as standard deviation of elevation and slope, and vegetation properties including LAI
533 and canopy height (Figures 8f and 8h). These factors are related to the radiation input and surface
534 properties, such as albedo and roughness length, which impact the energy cycles and availability
535 of ELR and ASR.



536

537 Figure 11. The spatial variability over each $0.5^\circ \times 0.5^\circ$ grid cell (left plots) and the top eight most

538 important drivers (right plots) of the spatial variability for SM, LH, ELR, and ASR. The inserted

539 histogram plot illustrates the probability distribution of the spatial variability across CONUS. The
540 relative importance of each variable in determining the spatial variability is calculated as the ratio
541 of the mean |SHAP value| of the variable to the sum of the mean |SHAP value| of all variables.
542 Therefore, the sum of the relative importance of all variables is 100%.

543

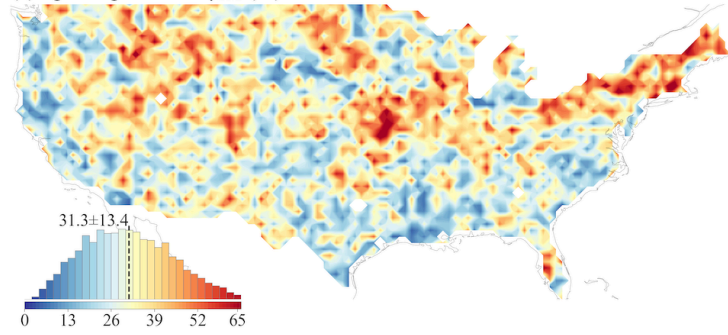
544 **3.6 The information loss of water and energy simulations and their drivers**

545 We also evaluated the information loss in simulations when upscaling from 1 km to 12 km
546 resolution and analyzed the drivers of their spatial patterns over CONUS. Four ML models were
547 built to explore the relationships between the γ of the simulations and its drivers including the γ of
548 the land surface parameters and the mean temperature and precipitation averaged over the $0.5^\circ \times$
549 0.5° box. These ML models performed well in predicting the simulations' γ , with small RMSE and
550 large R^2 (Figure S25).

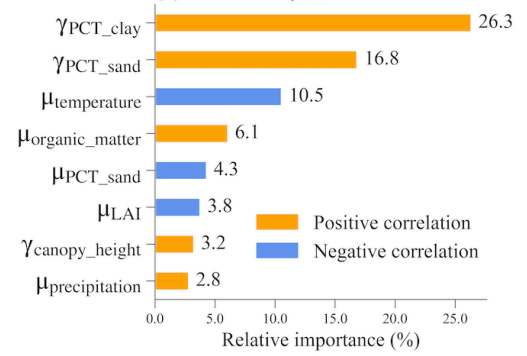
551 Significant information loss ranging from 31% to 54% with maximum values exceeding 90% is
552 observed for SM, LH, ELR, and ASR simulations (Figure 12). Their spatial patterns and drivers
553 show distinct variations. γ_{SM} is primarily driven by the information loss of percent clay and sand,
554 mean soil organic matter, and mean temperature, which affects the soil hydraulic properties and
555 soil water balance (Figures 9a and 9b). γ_{LH} displays high values in the eastern US and low values
556 in the western US (Figure 12c). It is primarily contributed by the information loss of vegetation
557 properties such as LAI and canopy height, and mean LAI, which influences the partitioning of LH
558 and sensible heat, and the partitioning of transpiration and evaporation (Figure 12d). γ_{ELR} exhibits
559 high values in the central and eastern US, particularly in the northeastern US, while γ_{ASR} has high
560 values almost all over the US, especially in the eastern regions (Figures 9e and 9g). γ_{ELR} and γ_{ASR}
561 are largely driven by vegetation properties such as LAI and canopy height, which are associated

562 with energy processes such as albedo (Figures 9f and 9h). Additionally, topography factors of
563 standard deviation of elevation and slope also slightly contribute to γ_{ASR} .

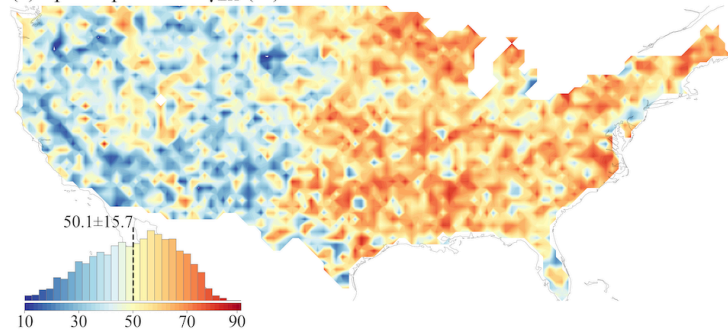
(a) Spatial pattern of γ_{SM} (%)



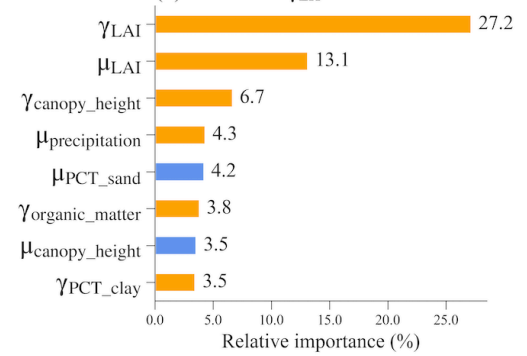
(b) Drivers of γ_{SM}



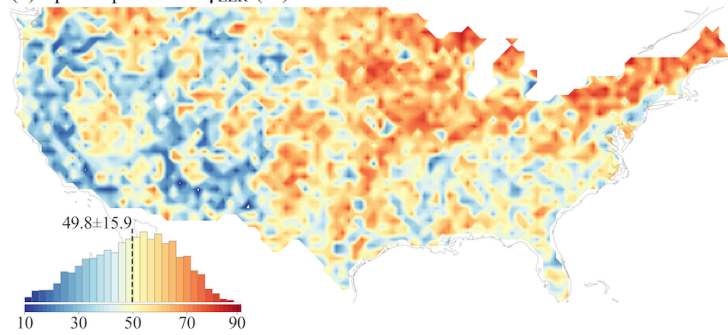
(c) Spatial pattern of γ_{LH} (%)



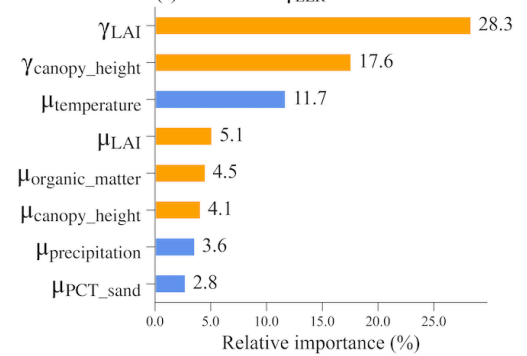
(d) Drivers of γ_{LH}



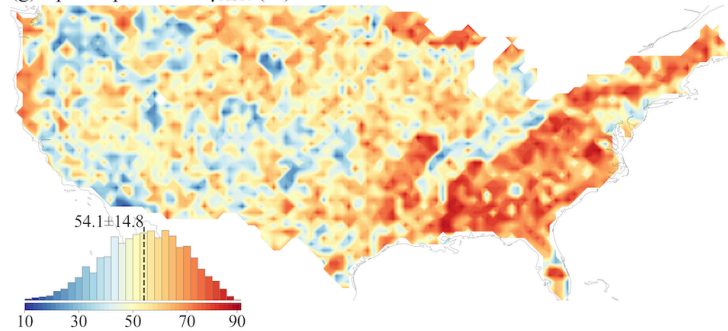
(e) Spatial pattern of γ_{ELR} (%)



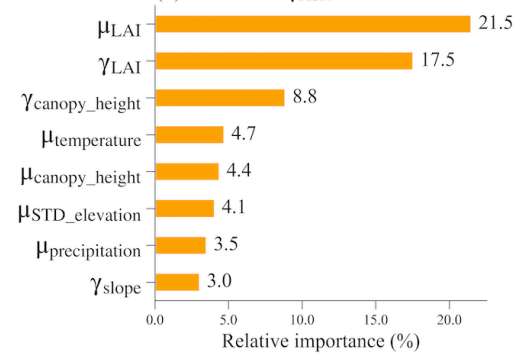
(f) Drivers of γ_{ELR}



(g) Spatial pattern of γ_{ASR} (%)



(h) Drivers of γ_{ASR}



564

565 Figure 12. Same to Figure 11 but for information loss.

566 **4. Discussion**

567 The development of new 1 km land surface parameter datasets in this study marks a substantial
568 improvement over commonly used land surface parameters such as CLM5 and K2012, leveraging
569 the latest high-resolution data sources with rigorous validation, including MODIS PFTs, enhanced
570 LAI and canopy height, soil properties, and topography factors. When compared with K2012 and
571 ELM2/CLM5 default datasets, the new 1k parameters exhibit notable differences, suggesting
572 potential improvement due to the use of more advanced data sources. Distinct features of the new
573 parameters include a reduction in bare soil compared to ELM2/CLM5, especially in regions like
574 North America and Central Asia, and diverse coverage of specific PFTs such as NDT and BET-
575 Tropical in areas like Siberia and South America. The LAI of the new parameters diverges from
576 K2012 and ELM2/CLM5, showing lower values in NET-Boreal PFT of the northern hemisphere
577 but higher BET-Tropical PFT in the tropics. The soil parameters, particularly in regions like
578 Europe, Central Asia, and the Western US, show significant differences between the new and
579 ELM2/CLM5 defaults. Moreover, the new parameters indicate larger slopes in mountainous
580 regions and more distinct elevation differences in areas such as Greenland and the Tibetan Plateau
581 compared to ELM2/CLM5. These differences potentially highlight enhanced accuracy and
582 sophistication of the new 1k parameters. Their enhanced resolution and rigorous validation suggest
583 a substantial capacity to improve ESMS modeling. Additionally, the richness of multi-year data
584 for LULC, LAI, and SAI in these datasets is especially valuable for examining land use and cover
585 changes, urbanization trends, deforestation impacts, and agricultural transformations.

586

587 The new 1 km land surface parameters can improve k-scale offline LSMs modeling by better
588 capturing spatial surface heterogeneity. As evidenced by the 1 km ELM simulation over CONUS,

589 soil properties, vegetation properties, and topographic factors contribute a lot to the spatial
590 heterogeneities of ELM water and energy simulations. Upscaling 1 km to a coarser 12 km
591 resolution, we observe significant spatial information loss, with SM experiencing an average loss
592 of 31%, and LH, ELR, and ASR experiencing around 50% information loss on average (Figure
593 12). This conclusion is in line with the results of Vergopolan et al. (2022), which showed a
594 substantial loss of spatial information in soil moisture when upscaling from 30 m to 1 km resolution,
595 with an average loss of approximately 48% and up to 80% over the CONUS region. The XML
596 analysis reveals that the spatial variability and information loss of ELM2 simulations are
597 influenced by the spatial variability and information loss of the different variables of land surface
598 parameters, as well as the mean precipitation and temperature (Figures 11 and 12). Our findings
599 highlight the critical role of land surface parameters in contributing to the spatial variability of
600 water and energy in land surface simulations, showcasing the value of the developed high-
601 resolution datasets. Another implementation example where our 1 km land surface parameters can
602 be beneficial is in hillslope-scale simulations, which are fundamental for organizing water, energy,
603 and biogeochemical processes (Fan et al., 2019). Krakauer et al. (2014) have highlighted the
604 significance of between-cell groundwater flow, which becomes comparable in magnitude to
605 recharge at grid spacings smaller than 10 km. Advancements have been made in ESMs to address
606 hillslope-scale processes, including the representation of intra-hillslope lateral subsurface flow
607 within grid cells in CLM5 (Swenson et al., 2019), the development of explicit lateral flow
608 processes between grid cells (Qiu et al., 2023), and the incorporation of topographic radiation
609 effects within and between grid cells (Hao et al., 2021). Another notable example is the integrated
610 hydrology-land surface model ParFlow-CLM, which incorporates three-dimensional groundwater
611 flow, two-dimensional overland flow, and land surface exchange processes (Maxwell, 2013).

612 ParFlow-CLM has demonstrated remarkable reliability in reproducing hydrologic processes, such
613 as its simulations at 3 km resolution for pan-European and 1 km resolution for CONUS (Naz et al.,
614 2023; O’Neill et al., 2021). More recently, Fang et al. (2022) coupled ParFlow with ELM and the
615 Functionally Assembled Terrestrial Ecosystem Simulator (FATES) to simulate carbon-hydrology
616 interactions at hillslope scale. By incorporating our 1 km datasets and leveraging these
617 advancements, we can improve simulations of hillslope-scale processes and enhance our
618 understanding of water and energy dynamics within ESMs.

619
620 Additionally, the new land surface parameters are also a timely resource for supporting the
621 emerging need for k-scale Earth system modeling, particularly in improving land-atmosphere
622 interaction processes. Representing the impact of spatial heterogeneity on land-atmosphere
623 interaction processes is a major challenge in Earth system modeling. Taking E3SM as an example,
624 researchers have proposed three key approaches to enhance spatial heterogeneity representation to
625 address this challenge. In line with these approaches, our newly developed 1 km land surface
626 parameters offer promising opportunities for improving land-atmosphere coupling within ESMs.
627 The first approach to enhance the representation of spatial heterogeneity is to directly conduct
628 simulations at high resolution. For instance, the Simple Cloud-Resolving E3SM Atmosphere
629 Model (SCREAM) has been used to perform global simulations at 3.25 km (Caldwell et al., 2021),
630 although the land surface parameters were based on coarser resolution datasets. By utilizing the
631 new 1 km land surface parameters, we can enhance the representation of land surface heterogeneity
632 within the ELM component of SCREAM, potentially improving modeling of land-atmosphere
633 coupling. The second and third approaches focus on improving the representation of land surface
634 heterogeneity within ESMs run at a coarse resolution while accounting for subgrid heterogeneity

635 in two different ways. In the second approach, the Cloud Layers Unified By Binormals (CLUBB)
636 has been implemented in E3SM Atmosphere Model (EAM) version 1 (Rasch et al., 2019;
637 Bogenschutz et al., 2013), to better account for subgrid atmospheric heterogeneity of turbulent
638 mixing, shallow convection, and cloud macrophysics. Recently, Huang et al. (2022) developed a
639 novel land-atmosphere coupling scheme in EAM that enables the communication of subgrid land
640 surface heterogeneity information to the atmosphere model with CLUBB, significantly impacting
641 boundary layer dynamics. The new 1km datasets can provide more accurate land surface
642 representations of the variability of individual patches and the inter-patch variability that were
643 used in Huang et al. (2022). The third approach is the Multiple Atmosphere Multiple Land (MAML)
644 approach used in the multiscale modeling framework (MMF) in which a cloud resolving model
645 (CRM) is embedded within each grid cell of the atmosphere (Baker et al., 2019; Lin et al., 2023;
646 Lee et al., 2023). In the MAML approach, each CRM column within the atmosphere grid is coupled
647 directly with its own independent land surface. This enables a more explicit representation of the
648 impact of spatial heterogeneity on land-atmosphere interactions within each grid and has shown
649 notable impacts on water and energy simulations (Baker et al., 2019; Lin et al., 2023). Lee et al.
650 (2023) highlighted the limitation of the current MAML approach, which utilizes the same land
651 surface characteristics for each land surface model interacting with the CRM column within the
652 same grid, which could lead to a weak representation of land-atmosphere interactions. To address
653 this limitation, incorporating the new 1 km land surface parameters within the MAML approach
654 can provide more detailed information about land surface heterogeneity, enabling a more accurate
655 capture of land-atmosphere interactions.

656

657 Evaluation of k-scale simulations, while essential, faces significant challenges as merely updating
658 the land surface input data to the new 1k parameters for k-scale simulations doesn't guarantee
659 improved model performance, which depends on both input data as well as model parameters and
660 structures. First, LSMs and ESMs that have been adapted for simulations at coarser resolutions
661 commensurate with the resolutions of previous land surface data require recalibration for effective
662 high-resolution modeling. This necessity for recalibration is echoed by Ruiz-Vásquez et al., (2023),
663 who noted that updating the ECMWF system with new land surface data did not inherently
664 improve performance, but improvements were seen after recalibrating key soil and vegetation-
665 related parameters. Second, high-resolution modeling requires the incorporation of new physical
666 processes crucial at finer scales. For example, hillslope-scale processes like lateral flow and
667 topography-radiation interactions are key to water and energy fluxes at high resolution (Han et al.,
668 2023; Hao et al., 2021). With increased heterogeneity at higher resolutions, larger differences in
669 land surface properties such as vegetation water use strategies requires more attention to plant
670 hydraulics besides the traditional focus on soil hydraulics for a more accurate depiction of plant
671 water use, as highlighted by Li et al., (2021). Third, the lack of high-resolution benchmarks for
672 large-scale applications, like k-scale atmospheric forcing data, remains a challenge, despite the
673 availability of relative coarse resolution global datasets such as ERA5_Land (Muñoz-Sabater et
674 al., 2021) and MSWX (Beck et al., 2021). Additionally, using soil moisture as an example, multiple
675 high-resolution datasets exhibit significantly different performance when compared to in-situ
676 measurements (Beck et al., 2021). Lastly, when evaluating simulations against benchmarks, it is
677 crucial not only to assess absolute differences using metrics like bias and root mean square error
678 but also to examine other metrics, such as the relationships between physical variables (e.g.,

679 rainfall vs. runoff; soil moisture vs. evapotranspiration), information loss, and the tail quantiles of
680 the probability distribution functions for simulations (e.g., extreme events).

681
682 There are certain opportunities for future development of 1k parameters. The urban extension may
683 vary based on data sources, urban definitions, and the algorithms employed, such as those derived
684 from harmonized nighttime lights (Zhao et al., 2022), global artificial impervious area (GAIA, Li
685 et al., 2020b; Gong et al., 2020), urban expansion (Liu et al., 2020; Kuang et al., 2021),
686 necessitating careful consideration in specific modeling applications. Additionally, urban
687 classification in J2010, based on global building height data, is limited by the lack of a consistent
688 and publicly accessible global dataset, despite available regional data for Europe (Frantz et al.,
689 2021), the US (Li et al., 2020a), and China (Cao and Huang, 2021; Yang and Zhao, 2022), thus
690 posing challenges to future urban classification enhancements. Incorporating local climate zones
691 offers a promising approach for urban classification and modeling. Moreover, the multiple-year
692 high-resolution PFT maps like the ones developed by the European Space Agency's Climate
693 Change Initiative could be used to further extend this dataset for a longer period (Harper et al.,
694 2023). Soil color, crucial for soil albedo and surface energy balance, lacks extensive global datasets
695 for ESMS modeling, but the global soil color map derived by Rizzo et al. (2023) offers potential
696 for further kilometer-scale ESMS and LSMS modeling.

697
698 The strategic aggregation of high-resolution parameters to coarser resolutions are crucial to
699 maintain accuracy and effectiveness in modeling applications. For instance, in soil properties, the
700 basic parameters (e.g., percent sand) are often utilized to derive secondary parameters (e.g.,
701 saturated water content). This aggregation procedure, whether performs before or after deriving

702 secondary parameters—known as 'aggregating first' and 'aggregating after'—is influenced by the
703 non-linear relationships between basic and derived parameters, with the latter method generally
704 preferred (Shangguan et al., 2014; Dai et al., 2019). Our study's initial approach in upscaling soil-
705 and topography-related parameters follows the 'aggregate first' approach, aligning with the
706 structure of models like ELM2 and CLM5. Conversely, models such as Common Land Model
707 (CoLM, Dai et al., 2003) and community Noah with multi-parameterization options (Noah-MP,
708 He et al., 2023; Niu et al., 2011; Yang et al., 2011) integrate secondary derived soil related
709 parameters directly as inputs, effectively demonstrating the advantages of the 'aggregating after'
710 approach. By leveraging secondary derived parameters from comprehensive databases such as
711 SoilGrids (Hengl et al., 2017) and GSDE (Shangguan et al., 2014), these models provide a valuable
712 framework for future development of models like ELM2 and CLM5 by directly integrating
713 secondary derived parameters.

714

715 **5. Data availability**

716 The 1 km land surface parameters are publicly available at
717 <https://doi.org/10.25584/PNNLDH/1986308> (Li et al., 2023).

718

719 **6. Conclusions**

720 We developed 1 km global land surface parameters using the latest available datasets covering
721 multiple years from 2001 to 2020. These parameters comprise four categories: LULC of PFTs and
722 non-vegetative land cover, vegetation properties, soil properties, and topographic factors. The new
723 1k parameters, when compared to the K2012 and ELM2/CLM5 default datasets, display
724 significant differences, indicating their potential superiority stemming from the utilization of latest
725 and more advanced data sources. The 1 km resolution ELM simulations conducted over CONUS
726 demonstrate the valuable capabilities of the new datasets in enabling k-scale land surface modeling.
727 Through scaling analysis of the 1 km resolution simulations within $0.5^\circ \times 0.5^\circ$ boxes where spatial
728 heterogeneity of the simulations is induced only by spatial heterogeneity of the land surface
729 parameters, we revealed the significant impact of land surface parameters on the spatial variability
730 of water and energy simulations. The spatial information loss of these simulations over CONUS
731 is significant when upscaling from 1 km to a coarser 12 km resolution, with an average ranging
732 from 31% to 54% and up to more than 90%. The XML analysis reveals that the spatial variability
733 and spatial information loss of ELM2 simulations are primarily impacted by the spatial variability
734 and information loss of soil properties, vegetation properties and topography factors, as well as the
735 mean climate conditions of precipitation and temperature. Furthermore, the spatial variability of
736 water and energy in the 1 km simulations is not dominated by the spatial heterogeneity of any land
737 surface parameters, suggesting the usefulness of the multi-parameter high-resolution land surface

738 parameter dataset. The availability of 1 km land surface parameters is a valuable resource that
739 addresses the emerging needs of k-scale LSMs and ESMs modeling. By providing accurate and
740 precise information, these 1 km land surface parameters will significantly enhance our
741 understanding of the water, carbon, and energy cycles under global change.

742

743 **Author contributions**

744 LL, GB, and DH designed the study, processed the datasets, conducted experiments, and drafted
745 the manuscript. LRL contributed to the conceptual design, discussion of results, and manuscript
746 revisions.

747

748 **Acknowledgments**

749 This study is supported by the US Department of Energy (DOE) Office of Science Biological and
750 Environmental Research as part of the Regional and Global Model Analysis (RGMA) program
751 area through the collaborative, multi-program Integrated Coastal Modeling (ICoM) project. This
752 study used DOE's Biological and Environmental Research Earth System Modeling program's
753 Compy computing cluster at Pacific Northwest National Laboratory. Pacific Northwest National
754 Laboratory is operated for the US Department of Energy by Battelle Memorial Institute under
755 contract DE-AC05-76RL01830. DH acknowledges the support from the US DOE, Office of
756 Science, Office of Biological and Environmental Research, Earth System Model Development
757 program area, as part of the Climate Process Team projects. Our thanks to Ye Liu and Teklu Tesfa
758 at PNNL for guidance on the canopy height dataset and K2012 datasets, respectively. We deeply
759 appreciate the reviewers for their valuable insights and suggestions.

760

761 **Financial support**

762 This work was supported by the Regional and Global Modeling and Analysis program area of the US
763 Department of Energy, Office of Science, Office of Biological and Environmental Research, as
764 part of the multi-program, collaborative integrated Coastal Modeling (ICoM) project (grant no.
765 KP1703110/75415).

766

767 **Competing interests**

768 At least one of the (co-)authors is a member of the editorial board of the Earth System Science

769 Data. The authors have no other competing interests to declare.

770 **Reference**

- 771 Arendt, A., Bliss, A., Bolch, T., et al.: Randolph Glacier Inventory—A Dataset of Global Glacier
772 Outlines Version: 1.0, Global Land Ice Measurements from Space, Boulder Colorado, USA.
773 Digital Media, 2012.
- 774 Baker, I. T., Denning, A. S., Dazlich, D. A., Harper, A. B., Branson, M. D., Randall, D. A.,
775 Phillips, M. C., Haynes, K. D., and Gallup, S. M.: Surface-Atmosphere Coupling Scale, the Fate
776 of Water, and Ecophysiological Function in a Brazilian Forest, *J Adv Model Earth Sy*, 11, 2523–
777 2546, <https://doi.org/10.1029/2019ms001650>, 2019.
- 778 Batjes, N.H.: ISRIC-WISE derived soil properties on a 5 by 5 arc-minutes global grid. Report
779 2006/02, available through : <http://www.isric.org>, 2006.
- 780 Beck, H. E., Van Dijk, A. I., Larraondo, P. R., McVicar, T. R., Pan, M., Dutra, E., & Miralles, D.
781 G.: MSWX: Global 3-hourly 0.1 bias-corrected meteorological data including near-real-time
782 updates and forecast ensembles, *BAMS*, 103(3), E710-E732, [https://doi.org/10.1175/BAMS-D-](https://doi.org/10.1175/BAMS-D-21-0145.1)
783 [21-0145.1](https://doi.org/10.1175/BAMS-D-21-0145.1), 2022.
- 784 Beck, H. E., Pan, M., Miralles, D. G., Reichle, R. H., Dorigo, W. A., Hahn, S., Sheffield, J.,
785 Karthikeyan, L., Balsamo, G., Parinussa, R. M., van Dijk, A. I. J. M., Du, J., Kimball, J. S.,
786 Vergopolan, N., and Wood, E. F.: Evaluation of 18 satellite- and model-based soil moisture
787 products using in situ measurements from 826 sensors, *Hydrol Earth Syst Sci*, 25, 17–40,
788 <https://doi.org/10.5194/hess-25-17-2021>, 2021.
- 789 Bogenschutz, P. A., Gettelman, A., Morrison, H., Larson, V. E., Craig, C., and Schanen, D. P.:
790 Higher-Order Turbulence Closure and Its Impact on Climate Simulations in the Community
791 Atmosphere Model, *J Climate*, 26, 9655–9676, <https://doi.org/10.1175/jcli-d-13-00075.1>, 2013.
- 792 Bonan, G. B., Oleson, K. W., Vertenstein, M., Levis, S., Zeng, X., Dai, Y., Dickinson, R. E., and
793 Yang, Z.-L.: The Land Surface Climatology of the Community Land Model Coupled to the
794 NCAR Community Climate Model*, *J Climate*, 15, 3123–3149, [https://doi.org/10.1175/1520-](https://doi.org/10.1175/1520-0442(2002)015<3123:tlscot>2.0.co;2)
795 [0442\(2002\)015<3123:tlscot>2.0.co;2](https://doi.org/10.1175/1520-0442(2002)015<3123:tlscot>2.0.co;2), 2002.
- 796 Bonan, G. B., Levis, S., Kergoat, L., & Oleson, K. W.: Landscapes as patches of plant functional
797 types: An integrating concept for climate and ecosystem models. *Global Biogeochemical Cycles*,
798 16(2), 5-1–5-23. <https://doi.org/10.1029/2000gb001360>, 2002
- 799 Bou-Zeid, E., Anderson, W., Katul, G. G., and Mahrt, L.: The Persistent Challenge of Surface
800 Heterogeneity in Boundary-Layer Meteorology: A Review, *Bound-lay Meteorol*, 177, 227–245,
801 <https://doi.org/10.1007/s10546-020-00551-8>, 2020.
- 802 Caldwell, P. M., Mametjanov, A., Tang, Q., Roedel, L. P. V., Golaz, J., Lin, W., Bader, D. C.,
803 Keen, N. D., Feng, Y., Jacob, R., Maltrud, M. E., Roberts, A. F., et al.: The DOE E3SM Coupled
804 Model Version 1: Description and Results at High Resolution, *J Adv Model Earth Sy*, 11, 4095–
805 4146, <https://doi.org/10.1029/2019ms001870>, 2019.

806 Caldwell, P. M., Terai, C. R., Hillman, B., Keen, N. D., Bogenschutz, P., Lin, W., et al.:
807 Convection-Permitting Simulations With the E3SM Global Atmosphere Model, *J Adv Model*
808 *Earth Sy*, 13, <https://doi.org/10.1029/2021ms002544>, 2021.

809 Cao, Y. and Huang, X.: A deep learning method for building height estimation using high-
810 resolution multi-view imagery over urban areas: A case study of 42 Chinese cities, *Remote Sens*
811 *Environ*, 264, 112590, <https://doi.org/10.1016/j.rse.2021.112590>, 2021.

812 Chaney, N. W., Huijgevoort, M. H. J. V., Shevliakova, E., Malyshev, S., Milly, P. C. D.,
813 Gauthier, P. P. G., and Sulman, B. N.: Harnessing big data to rethink land heterogeneity in Earth
814 system models, *Hydrol Earth Syst Sc*, 22, 3311–3330, [https://doi.org/10.5194/hess-22-3311-](https://doi.org/10.5194/hess-22-3311-2018)
815 [2018](https://doi.org/10.5194/hess-22-3311-2018), 2018.

816 Change, N. C.: Think big and model small, *Nat Clim Change*, 12, 493–493,
817 <https://doi.org/10.1038/s41558-022-01399-1>, 2022.

818 Chen, T. and Guestrin, C.: XGBoost: A Scalable Tree Boosting System, *Proc 22nd Acm Sigkdd*
819 *Int Conf Knowl Discov Data Min*, 785–794, <https://doi.org/10.1145/2939672.2939785>, 2016.

820 Dai, Y., Zeng, X., Dickinson, R. E., Baker, I., Bonan, G. B., Bosilovich, M. G., et al.: The
821 common land model, *BAMS*, 84(8), 1013-1024, <https://doi.org/10.1175/BAMS-84-8-1013>,
822 2003.

823 Dai, Y., Shangguan, W., Wei, N., Xin, Q., Yuan, H., Zhang, S., Liu, S., Lu, X., Wang, D., and
824 Yan, F.: A Review of the Global Soil Property Maps for Earth System Models, *SOIL*, 5, 137-
825 158. <https://doi.org/10.5194/soil-5-137-2019>, 2019.

826 Defries, R. S., Hansen, M. C., Townshend, J. R. G., Janetos, A. C., and Loveland, T. R.: A new
827 global 1-km dataset of percentage tree cover derived from remote sensing: GLOBAL
828 PERCENTAGE TREE COVER FROM REMOTE SENSING, *Global Change Biol*, 6, 247–254,
829 <https://doi.org/10.1046/j.1365-2486.2000.00296.x>, 2000.

830 Dozier, J.: Revisiting Topographic Horizons in the Era of Big Data and Parallel Computing, *Ieee*
831 *Geosci Remote S*, 19, 1–5, <https://doi.org/10.1109/lgrs.2021.3125278>, 2022.

832 Fan, Y., Clark, M., Lawrence, D. M., Swenson, S., Band, L. E., Brantley, S. L., et al.: Hillslope
833 Hydrology in Global Change Research and Earth System Modeling, *Water Resour Res*, 55,
834 1737–1772, <https://doi.org/10.1029/2018wr023903>, 2019.

835 Frantz, D., Schug, F., Okujeni, A., Navacchi, C., Wagner, W., Linden, S. van der, and Hostert,
836 P.: National-scale mapping of building height using Sentinel-1 and Sentinel-2 time series,
837 *Remote Sens Environ*, 252, 112128, <https://doi.org/10.1016/j.rse.2020.112128>, 2021.

838 Friedl, M. A., McIver, D. K., Hodges, J. C. F., Zhang, X. Y., Muchoney, D., Strahler, A. H.,
839 Woodcock, C. E., Gopal, S., Schneider, A., Cooper, A., Baccini, A., Gao, F., and Schaaf, C.:

840 Global land cover mapping from MODIS: algorithms and early results, *Remote Sens Environ*,
841 83, 287–302, [https://doi.org/10.1016/s0034-4257\(02\)00078-0](https://doi.org/10.1016/s0034-4257(02)00078-0), 2002.

842 Friedl, M. A., Sulla-Menashe, D., Tan, B., Schneider, A., Ramankutty, N., Sibley, A., and
843 Huang, X.: MODIS Collection 5 global land cover: Algorithm refinements and characterization
844 of new datasets, *Remote Sens Environ*, 114, 168–182, <https://doi.org/10.1016/j.rse.2009.08.016>,
845 2010.

846 Friedl, M., Sulla-Menashe, D.: MCD12Q1 MODIS/Terra+Aqua Land Cover Type Yearly L3
847 Global 500m SIN Grid V006 [Data set]. NASA EOSDIS Land Processes DAAC. Accessed
848 2022-11-21 from <https://doi.org/10.5067/MODIS/MCD12Q1.006>, 2019.

849 Giorgi, F. and Avissar, R.: Representation of heterogeneity effects in Earth system modeling:
850 Experience from land surface modeling, *Rev Geophys*, 35, 413–437,
851 <https://doi.org/10.1029/97rg01754>, 1997.

852 Gorelick, N., Hancher, M., Dixon, M., Ilyushchenko, S., Thau, D., & Moore, R.: Google Earth
853 Engine: Planetary-scale geospatial analysis for everyone. *Remote Sensing of Environment*, 202,
854 18–27. <https://doi.org/10.1016/j.rse.2017.06.031>, 2017.

855 Gong, P., Li, X., Wang, J., Bai, Y., Chen, B., Hu, T., Liu, X., Xu, B., Yang, J., Zhang, W., and
856 Zhou, Y.: Annual maps of global artificial impervious area (GAIA) between 1985 and 2018,
857 *Remote Sens Environ*, 236, 111510, <https://doi.org/10.1016/j.rse.2019.111510>, 2020.

858 Gorelick, N., Hancher, M., Dixon, M., Ilyushchenko, S., Thau, D., and Moore, R.: Google Earth
859 Engine: Planetary-scale geospatial analysis for everyone, *Remote Sens Environ*, 202, 18–27,
860 <https://doi.org/10.1016/j.rse.2017.06.031>, 2017.

861 Hansen, M. C., DeFries, R. S., Townshend, J. R. G., Carroll, M., Dimiceli, C., and Sohlberg, R.
862 A.: Global Percent Tree Cover at a Spatial Resolution of 500 Meters: First Results of the MODIS
863 Vegetation Continuous Fields Algorithm, *Earth Interact*, 7, 1–15, [https://doi.org/10.1175/1087-3562\(2003\)007<;0001:gptcaa>2.0.co;2](https://doi.org/10.1175/1087-3562(2003)007<;0001:gptcaa>2.0.co;2), 2003.

865 Hao, D., Bisht, G., Huang, M., Ma, P., Tesfa, T., Lee, W., Gu, Y., and Leung, L. R.: Impacts of
866 Sub-Grid Topographic Representations on Surface Energy Balance and Boundary Conditions in
867 the E3SM Land Model: A Case Study in Sierra Nevada, *J Adv Model Earth Sy*, 14,
868 <https://doi.org/10.1029/2021ms002862>, 2022.

869 Harper, K. L., Lamarche, C., Hartley, A., Peylin, P., Ottlé, C., Bastrikov, V., Martín, R. S.,
870 Bohnenstengel, S. I., Kirches, G., Boettcher, M., Shevchuk, R., Brockmann, C., and Defourny,
871 P.: A 29-year time series of annual 300 m resolution plant-functional-type maps for climate
872 models, *Earth Syst Sci Data*, 15, 1465–1499, <https://doi.org/10.5194/essd-15-1465-2023>, 2023.

873 Hengl, T., Jesus, J. M. de, Heuvelink, G. B. M., Gonzalez, M. R., Kilibarda, M., Blagotić, A.,
874 Shangquan, W., Wright, M. N., et al.: SoilGrids250m: Global gridded soil information based on
875 machine learning, *Plos One*, 12, e0169748, <https://doi.org/10.1371/journal.pone.0169748>, 2017.

876 Hewitt, H., Fox-Kemper, B., Pearson, B., Roberts, M., and Klocke, D.: The small scales of the
877 ocean may hold the key to surprises, *Nat Clim Change*, 12, 496–499,
878 <https://doi.org/10.1038/s41558-022-01386-6>, 2022.

879 He, C., Valayamkunnath, P., Barlage, M., Chen, F., Gochis, D., Cabell, R., Schneider, T.,
880 Rasmussen, R., Niu, G.-Y., Yang, Z.-L., Niyogi, D., and Ek, M.: Modernizing the open-source
881 community Noah with multi-parameterization options (Noah-MP) land surface model (version
882 5.0) with enhanced modularity, interoperability, and applicability, *Geosci Model Dev*, 16, 5131–
883 5151, <https://doi.org/10.5194/gmd-16-5131-2023>, 2023.

884 Hijmans, R. J., Cameron, S. E., Parra, J. L., Jones, P. G., and Jarvis, A.: Very high resolution
885 interpolated climate surfaces for global land areas, *International Journal of Climatology*, 25,
886 1965–1978, <https://doi.org/10.1002/joc.1276>, 2005.

887 Hu, Z., Islam, S., and Cheng, Y.: Statistical characterization of remotely sensed soil moisture
888 images, *Remote Sens Environ*, 61, 310–318, [https://doi.org/10.1016/s0034-4257\(97\)89498-9](https://doi.org/10.1016/s0034-4257(97)89498-9),
889 1997.

890 Huang, M., Ma, P.-L., Chaney, N. W., Hao, D., Bisht, G., Fowler, M. D., Larson, V. E., and
891 Leung, L. R.: Representing surface heterogeneity in land-atmosphere coupling in E3SMv1
892 single-column model over ARM SGP during summertime, *Geoscientific Model Dev Discuss*,
893 2022, 1–20, <https://doi.org/10.5194/gmd-2021-421>, 2022.

894 Huang, F., Jiang, S., Zhan, W., Bechtel, B., Liu, Z., Demuzere, M.: Mapping local climate zones
895 for cities: A large review, *Remote Sens. Environ.*, 292, 113573,
896 <https://doi.org/10.1016/j.rse.2023.113573>, 2023.

897 Hugelius, G., Tarnocai, C., Broll, G., Canadell, J. G., Kuhry, P., and Swanson, D. K.: The
898 Northern Circumpolar Soil Carbon Database: spatially distributed datasets of soil coverage and
899 soil carbon storage in the northern permafrost regions, *Earth Syst. Sci. Data*, 5, 3–13,
900 <https://doi.org/10.5194/essd-5-3-2013>, 2013.

901 IGBP: Global Soil Data Task (IGBP-DIS, ISO-image of CD). International Geosphere-Biosphere
902 Program, PANGAEA, <https://doi.org/10.1594/PANGAEA.869912>, 2000.

903 Jackson, T. L., Feddema, J. J., Oleson, K. W., Bonan, G. B., and Bauer, J. T.: Parameterization
904 of Urban Characteristics for Global Climate Modeling, *Ann Assoc Am Geogr*, 100, 848–865,
905 <https://doi.org/10.1080/00045608.2010.497328>, 2010.

906 Jarvis, A., H.I. Reuter, A. Nelson, E. Guevara.: Hole-filled SRTM for the globe Version 4,
907 available from the CGIAR-CSI SRTM 90m Database: <https://srtm.csi.cgiar.org>, 2008.

908 Ji, P. and Yuan, X.: High-Resolution Land Surface Modeling of Hydrological Changes Over the
909 Sanjiangyuan Region in the Eastern Tibetan Plateau: 2. Impact of Climate and Land Cover
910 Change, *J Adv Model Earth Sy*, 10, 2829–2843, <https://doi.org/10.1029/2018ms001413>, 2018.

- 911 Ji, P., Yuan, X., Shi, C., Jiang, L., Wang, G., and Yang, K.: A Long-Term Simulation of Land
912 Surface Conditions at High Resolution over Continental China, *J Hydrometeorol*, 24, 285–314,
913 <https://doi.org/10.1175/jhm-d-22-0135.1>, 2023.
- 914 Ke, Y., Leung, L. R., Huang, M., Coleman, A. M., Li, H., and Wigmosta, M. S.: Development of
915 high resolution land surface parameters for the Community Land Model, *Geosci Model Dev*, 5,
916 1341–1362, <https://doi.org/10.5194/gmd-5-1341-2012>, 2012.
- 917 Ke, Y., Leung, L. R., Huang, M., and Li, H.: Enhancing the representation of subgrid land
918 surface characteristics in land surface models, *Geosci Model Dev*, 6, 1609–1622,
919 <https://doi.org/10.5194/gmd-6-1609-2013>, 2013.
- 920 Kim, H.: Global Soil Wetness Project Phase 3 Atmospheric Boundary Conditions (Experiment 1)
921 [Data set]. Data Integration and Analysis System (DIAS). <https://doi.org/10.20783/DIAS.501>,
922 2017.
- 923 Kourzeneva, E.: Global dataset for the parameterization of lakes in Numerical Weather
924 Prediction and Climate modeling. ALADIN Newsletter, No 37, July-December, 2009, F.
925 Bouttier and C. Fischer, Eds., Meteo-France, Toulouse, France, 46-53, 2009.
- 926 Kourzeneva, E.: External data for lake parameterization in Numerical Weather Prediction and
927 climate modeling. *Boreal Environment Research*, 15, 165-177, 2010.
- 928 Krakauer, N. Y., Li, H., and Fan, Y.: Groundwater flow across spatial scales: importance for
929 climate modeling, *Environ Res Lett*, 9, 034003, <https://doi.org/10.1088/1748-9326/9/3/034003>,
930 2014.
- 931 Kuang, W., Du, G., Lu, D., Dou, Y., Li, X., Zhang, S., Chi, W., Dong, J., Chen, G., Yin, Z., Pan,
932 T., Hamdi, R., Hou, Y., Chen, C., Li, H., and Miao, C.: Global observation of urban expansion
933 and land-cover dynamics using satellite big-data, *Sci Bull*, 66, 297–300,
934 <https://doi.org/10.1016/j.scib.2020.10.022>, 2021.
- 935 Lang, N., Jetz, W., Schindler, K., and Wegner, J. D.: A high-resolution canopy height model of
936 the Earth. *Nat Ecol Evol*, <https://doi.org/10.1038/s41559-023-02206-6>, 2023.
- 937 Lawrence, D. M., Fisher, R. A., Koven, C. D., Oleson, K. W., Swenson, S. C., Bonan, G., et al.:
938 The Community Land Model Version 5: Description of New Features, Benchmarking, and
939 Impact of Forcing Uncertainty, *J Adv Model Earth Sy*, 11, 4245–4287,
940 <https://doi.org/10.1029/2018ms001583>, 2019.
- 941 Lawrence, D., Fisher, R., Koven, C., Oleson, K., Swenson, S., et al. (2018). Technical
942 description of version 5.0 of the Community Land Model (CLM). National Center for
943 Atmospheric Research, University Corporation for Atmospheric Research, Boulder, CO.
944 https://escomp.github.io/ctsm-docs/versions/release-clm5.0/html/tech_note/index.html

- 945 Lee, J., Hannah, W. M., and Bader, D. C.: Representation of atmosphere induced heterogeneity
946 in land – atmosphere interactions in E3SM-MMFv2, *Geoscientific Model Dev Discuss*, 2023, 1–
947 21, <https://doi.org/10.5194/gmd-2023-55>, 2023.
- 948 Leng, G., Huang, M., Tang, Q., Sacks, W. J., Lei, H., and Leung, L. R.: Modeling the effects of
949 irrigation on land surface fluxes and states over the conterminous United States: Sensitivity to
950 input data and model parameters, *J Geophys Res Atmospheres*, 118, 9789–9803,
951 <https://doi.org/10.1002/jgrd.50792>, 2013.
- 952 Leung, L. R., Bader, D. C., Taylor, M. A., and McCoy, R. B.: An Introduction to the E3SM
953 Special Collection: Goals, Science Drivers, Development, and Analysis, *J Adv Model Earth Sy*,
954 12, <https://doi.org/10.1029/2019ms001821>, 2020.
- 955 Li, L., Yang, Z., Matheny, A. M., Zheng, H., Swenson, S. C., Lawrence, D. M., Barlage, M.,
956 Yan, B., McDowell, N. G., and Leung, L. R.: Representation of Plant Hydraulics in the Noah-
957 MP Land Surface Model: Model Development and Multiscale Evaluation, *J Adv Model Earth*
958 *Sy*, 13, <https://doi.org/10.1029/2020ms002214>, 2021.
- 959 Li, L., Bisht, G., and Leung, L. R.: Spatial heterogeneity effects on land surface modeling of
960 water and energy partitioning, *Geosci Model Dev*, 15, 5489–5510, <https://doi.org/10.5194/gmd-15-5489-2022>, 2022.
- 962 Li, X., Zhou, Y., Gong, P., Seto, K. C., and Clinton, N.: Developing a method to estimate
963 building height from Sentinel-1 data, *Remote Sens Environ*, 240, 111705,
964 <https://doi.org/10.1016/j.rse.2020.111705>, 2020a.
- 965 Li, X., Gong, P., Zhou, Y., Wang, J., Bai, Y., Chen, B., Hu, T., Xiao, Y., et al.: Mapping global
966 urban boundaries from the global artificial impervious area (GAIA) data, *Environ Res Lett*, 15,
967 094044, <https://doi.org/10.1088/1748-9326/ab9be3>, 2020b.
- 968 Li, L., Bisht, G., Hao, D., Leung, L.R.: Global 1km Land Surface Parameters for Kilometer
969 Scale Earth System Modeling, Pacific Northwest National Laboratory DataHub [data set],
970 <https://doi.org/10.25584/PNNLDH/1986308>, 2023.
- 971 Lin, G., Leung, L. R., Lee, J., Harrop, B. E., Baker, I. T., Branson, M. D., Denning, A. S., Jones,
972 C. R., Ovchinnikov, M., Randall, D. A., and Yang, Z.: Modeling Land-Atmosphere Coupling at
973 Cloud-Resolving Scale Within the Multiple Atmosphere Multiple Land (MAML) Framework in
974 SP-E3SM, *J Adv Model Earth Sy*, 15, <https://doi.org/10.1029/2022ms003101>, 2023.
- 975 Liu, S., Shao, Y., Kunoth, A., and Simmer, C.: Impact of surface-heterogeneity on atmosphere
976 and land-surface interactions, *Environ Modell Softw*, 88, 35–47,
977 <https://doi.org/10.1016/j.envsoft.2016.11.006>, 2017.
- 978 Liu, X., Huang, Y., Xu, X., Li, X., Li, X., Ciais, P., Lin, P., et al.: High-spatiotemporal-
979 resolution mapping of global urban change from 1985 to 2015, *Nat Sustain*, 3, 564–570,
980 <https://doi.org/10.1038/s41893-020-0521-x>, 2020.

- 981 Lundberg, S. and Lee, S.-I.: A Unified Approach to Interpreting Model Predictions, Arxiv, 2017.
- 982 Lundberg, S. M., Nair, B., Vavilala, M. S., Horibe, M., Eisses, M. J., Adams, T., Liston, D. E.,
983 Low, D. K.-W., Newman, S.-F., Kim, J., and Lee, S.-I.: Explainable machine-learning
984 predictions for the prevention of hypoxaemia during surgery, *Nat Biomed Eng*, 2, 749–760,
985 <https://doi.org/10.1038/s41551-018-0304-0>, 2018.
- 986 Lundberg, S. M., Erion, G., Chen, H., DeGrave, A., Prutkin, J. M., Nair, B., Katz, R.,
987 Himmelfarb, J., Bansal, N., and Lee, S.-I.: From local explanations to global understanding with
988 explainable AI for trees, *Nat Mach Intell*, 2, 56–67, <https://doi.org/10.1038/s42256-019-0138-9>,
989 2020.
- 990 Mälicke, M., Hassler, S. K., Blume, T., Weiler, M., and Zehe, E.: Soil moisture: variable in
991 space but redundant in time, *Hydrol Earth Syst Sc*, 24, 2633–2653, [https://doi.org/10.5194/hess-](https://doi.org/10.5194/hess-24-2633-2020)
992 [24-2633-2020](https://doi.org/10.5194/hess-24-2633-2020), 2020.
- 993 Maxwell, R. M.: A terrain-following grid transform and preconditioner for parallel, large-scale,
994 integrated hydrologic modeling, *Adv Water Resour*, 53, 109–117,
995 <https://doi.org/10.1016/j.advwatres.2012.10.001>, 2013.
- 996 Morisette, J. T., Baret, F., Privette, J. L., Myneni, R. B., Nickeson, J. E., et al.: Validation of
997 global moderate-resolution LAI products: A framework proposed within the CEOS land product
998 validation subgroup, *IEEE Trans Geosci Remote Sens*, 44(7), 1804–1817.
999 <https://doi.org/10.1109/TGRS.2006.872529>, 2006.
- 1000 Muñoz-Sabater, J., Dutra, E., Agustí-Panareda, A., Albergel, C., Arduini, G., Balsamo, G.,
1001 Boussetta, S., Choulga, M., Harrigan, S., Hersbach, H., Martens, B., Miralles, D. G., Piles, M.,
1002 Rodríguez-Fernández, N. J., Zsoter, E., Buontempo, C., and Thépaut, J.-N.: ERA5-Land: a state-
1003 of-the-art global reanalysis dataset for land applications, *Earth Syst Sci Data*, 13, 4349–4383,
1004 <https://doi.org/10.5194/essd-13-4349-2021>, 2021.
- 1005 Myneni, R. B., Hoffman, S., Knyazikhin, Y., Privette, J. L., Glassy, J., Tian, Y., Wang, Y., Song,
1006 X., Zhang, Y., Smith, G. R., Lotsch, A., Friedl, M., Morisette, J. T., Votava, P., Nemani, R. R.,
1007 and Running, S. W.: Global products of vegetation leaf area and fraction absorbed PAR from
1008 year one of MODIS data, *Remote Sens Environ*, 83, 214–231, [https://doi.org/10.1016/s0034-](https://doi.org/10.1016/s0034-4257(02)00074-3)
1009 [4257\(02\)00074-3](https://doi.org/10.1016/s0034-4257(02)00074-3), 2002.
- 1010 Myneni, R., Knyazikhin, Y., Park, T. (2021). MODIS/Terra+Aqua Leaf Area Index/FPAR 4-Day
1011 L4 Global 500m SIN Grid V061 [Data set]. NASA EOSDIS Land Processes DAAC. Accessed
1012 2022-11-21 from <https://doi.org/10.5067/MODIS/MCD15A3H.061>
- 1013 Naz, B. S., Sharples, W., Ma, Y., Goergen, K., and Kollet, S.: Continental-scale evaluation of a
1014 fully distributed coupled land surface and groundwater model, ParFlow-CLM (v3.6.0), over
1015 Europe, *Geosci Model Dev*, 16, 1617–1639, <https://doi.org/10.5194/gmd-16-1617-2023>, 2023.

- 1016 Niu, G. Y., Yang, Z. L., Mitchell, K. E., Chen, F., Ek, M. B., Barlage, M., et al.: The community
1017 Noah land surface model with multiparameterization options (Noah-MP): 1. Model description
1018 and evaluation with local-scale measurements, *J Geophys Res Atmos*, 116(D12),
1019 <https://doi.org/10.1029/2010JD015139>, 2011
- 1020 O'Neill, M. M. F., Tijerina, D. T., Condon, L. E., and Maxwell, R. M.: Assessment of the
1021 ParFlow-CLM CONUS 1.0 integrated hydrologic model: evaluation of hyper-resolution water
1022 balance components across the contiguous United States, *Geosci Model Dev*, 14, 7223–7254,
1023 <https://doi.org/10.5194/gmd-14-7223-2021>, 2021.
- 1024 Poggio, L., Sousa, L. M. de, Batjes, N. H., Heuvelink, G. B. M., Kempen, B., Ribeiro, E., and
1025 Rossiter, D.: SoilGrids 2.0: producing soil information for the globe with quantified spatial
1026 uncertainty, *Soil*, 7, 217–240, <https://doi.org/10.5194/soil-7-217-2021>, 2021.
- 1027 Qiu, H., Bisht, G., Li, L., Hao, D., and Xu, D.: Development of Inter-Grid Cell Lateral
1028 Unsaturated and Saturated Flow Model in the E3SM Land Model (v2.0), *Egusphere*, 2023, 1–31,
1029 <https://doi.org/10.5194/egusphere-2023-375>, 2023.
- 1030 Rabus, B., Eineder, M., Roth, A., & Bamler, R.: The shuttle radar topography mission—A new
1031 class of digital elevation models acquired by spaceborne radar. *ISPRS Journal of*
1032 *Photogrammetry and Remote Sensing*, 57(4), 241–262. [https://doi.org/10.1016/s0924-](https://doi.org/10.1016/s0924-2716(02)00124-7)
1033 [2716\(02\)00124-7](https://doi.org/10.1016/s0924-2716(02)00124-7), 2003.
- 1034 Ramankutty, N. and Foley, J. A.: Estimating historical changes in global land cover: Croplands
1035 from 1700 to 1992, *Global Biogeochem Cy*, 13, 997–1027,
1036 <https://doi.org/10.1029/1999gb900046>, 1999.
- 1037 Rasch, P. J., Xie, S., Ma, P. -L., Lin, W., Wang, H., Tang, Q., Burrows, S. M., Caldwell, P., et
1038 al.: An Overview of the Atmospheric Component of the Energy Exascale Earth System Model, *J*
1039 *Adv Model Earth Sy*, 11, 2377–2411, <https://doi.org/10.1029/2019ms001629>, 2019.
- 1040 Rastner, P., Bolch, T., Mölg, N., Machguth, H., Le Bris, R., and Paul, F.: The first complete
1041 inventory of the local glaciers and ice caps on Greenland, *The Cryosphere*, 6, 1483–1495,
1042 <https://doi.org/10.5194/tc-6-1483-2012>, 2012.
- 1043 Rizzo, R., Wadoux, A. M. C., Demattê, J. A., Minasny, B., Barrón, V., Ben-Dor, E., ... &
1044 Salama, E. S. M.: Remote sensing of the Earth's soil color in space and time, *Remote Sens*
1045 *Environ*, 299, 113845, <https://doi.org/10.1016/j.rse.2023.113845>, 2023.
- 1046 Rouf, T., Maggioni, V., Mei, Y., and Houser, P.: Towards hyper-resolution land-surface
1047 modeling of surface and root zone soil moisture, *J Hydrol*, 594, 125945,
1048 <https://doi.org/10.1016/j.jhydrol.2020.125945>, 2021.
- 1049 Ruiz-Vásquez, M., O, S., Arduini, G., Boussetta, S., Brenning, A., et al: Impact of updating
1050 vegetation information on land surface model performance, *J. Geophys. Res. Atmos.*, 128(21),
1051 e2023JD039076, <https://doi.org/10.1029/2023JD039076>, 2023.

- 1052 Shangguan, W., Dai, Y., Duan, Q., Liu, B., and Yuan, H.: A Global Soil Dataset for Earth
1053 System Modeling, *J Adv Model Earth Syst*, 6, 249-263, <https://doi.org/10.1002/2013MS000293>,
1054 2014.
- 1055 Simard, M., Pinto, N., Fisher, J. B., and Baccini, A.: Mapping forest canopy height globally with
1056 spaceborne lidar, *J. Geophys. Res. Biogeosci.*, 116, G04021,
1057 <https://doi.org/10.1029/2011jg001708>, 2011.
- 1058 Singh, R. S., Reager, J. T., Miller, N. L., and Famiglietti, J. S.: Toward hyper-resolution land-
1059 surface modeling: The effects of fine-scale topography and soil texture on CLM4.0 simulations
1060 over the Southwestern U.S., *Water Resour Res*, 51, 2648–2667,
1061 <https://doi.org/10.1002/2014wr015686>, 2015.
- 1062 Slingo, J., Bates, P., Bauer, P., Belcher, S., Palmer, T., Stephens, G., Stevens, B., Stocker, T.,
1063 and Teutsch, G.: Ambitious partnership needed for reliable climate prediction, *Nat Clim Change*,
1064 12, 499–503, <https://doi.org/10.1038/s41558-022-01384-8>, 2022.
- 1065 Still, C. J., Berry, J. A., Collatz, G. J., and DeFries, R. S.: Global distribution of C3 and C4
1066 vegetation: Carbon cycle implications, *Global Biogeochem Cy*, 17, 6-1-6–14,
1067 <https://doi.org/10.1029/2001gb001807>, 2003.
- 1068 Sulla-Menashe, D., Gray, J. M., Abercrombie, S. P., and Friedl, M. A.: Hierarchical mapping of
1069 annual global land cover 2001 to present: The MODIS Collection 6 Land Cover product, *Remote
1070 Sens Environ*, 222, 183–194, <https://doi.org/10.1016/j.rse.2018.12.013>, 2019.
- 1071 Swenson, S. C., Clark, M., Fan, Y., Lawrence, D. M., and Perket, J.: Representing Intrahillslope
1072 Lateral Subsurface Flow in the Community Land Model, *J Adv Model Earth Sy*, 11, 4044–4065,
1073 <https://doi.org/10.1029/2019ms001833>, 2019.
- 1074 Verdin, K. L. and Greenlee, S. K.: Development of continental scale digital elevation models and
1075 extraction of hydrographic features, paper presented at the Third International Workshop on
1076 Integrating GIS and Environmental Modeling, Santa Fe, New Mexico, 21–26 January, Natl.
1077 Cent. for Geogr. Inf. and Anal., Santa Barbara, Calif, 1996.
- 1078 Vergopolan, N., Chaney, N. W., Beck, H. E., Pan, M., Sheffield, J., Chan, S., and Wood, E. F.:
1079 Combining hyper-resolution land surface modeling with SMAP brightness temperatures to
1080 obtain 30-m soil moisture estimates, *Remote Sens Environ*, 242, 111740,
1081 <https://doi.org/10.1016/j.rse.2020.111740>, 2020.
- 1082 Vergopolan, N., Chaney, N. W., Pan, M., Sheffield, J., Beck, H. E., Ferguson, C. R., Torres-
1083 Rojas, L., Sadri, S., and Wood, E. F.: SMAP-HydroBlocks, a 30-m satellite-based soil moisture
1084 dataset for the conterminous US, *Sci Data*, 8, 264, <https://doi.org/10.1038/s41597-021-01050-2>,
1085 2021.
- 1086 Vergopolan, N., Sheffield, J., Chaney, N. W., Pan, M., Beck, H. E., Ferguson, C. R., Torres-
1087 Rojas, L., Eigenbrod, F., Crow, W., and Wood, E. F.: High-Resolution Soil Moisture Data

- 1088 Reveal Complex Multi-Scale Spatial Variability Across the United States, *Geophys Res Lett*, 49,
1089 <https://doi.org/10.1029/2022gl098586>, 2022.
- 1090 Wood, E. F., Roundy, J. K., Troy, T. J., Beek, L. P. H. van, Bierkens, M. F. P., et al.:
1091 Hyperresolution global land surface modeling: Meeting a grand challenge for monitoring Earth's
1092 terrestrial water, *Water Resour Res*, 47, <https://doi.org/10.1029/2010wr010090>, 2011.
- 1093 Xia, Y., Mocko, D., Huang, M., Li, B., Rodell, M., Mitchell, K. E., Cai, X., and Ek, M. B.:
1094 Comparison and Assessment of Three Advanced Land Surface Models in Simulating Terrestrial
1095 Water Storage Components over the United States, *J Hydrometeorol*, 18, 625–649,
1096 <https://doi.org/10.1175/jhm-d-16-0112.1>, 2017.
- 1097 Xu, C., Torres-Rojas, L., Vergopolan, N., Chaney, N. W.: The Benefits of Using State-Of-The-
1098 Art Digital Soil Properties Maps to Improve the Modeling of Soil Moisture in Land Surface
1099 Models, *Water Resour Res*, 59(4), e2022WR032336, <https://doi.org/10.1029/2022WR032336>,
1100 2023.
- 1101 Yang, Z. L., Niu, G. Y., Mitchell, K. E., Chen, F., Ek, M. B., Barlage, M., et al.: The community
1102 Noah land surface model with multiparameterization options (Noah-MP): 2. Evaluation over
1103 global river basins, *J Geophys Res Atmos*, 116(D12), <https://doi.org/10.1029/2010JD015140>,
1104 2011.
- 1105 Yamazaki, D., Ikeshima, D., Sosa, J., Bates, P. D., Allen, G. H., and Pavelsky, T. M.: MERIT
1106 Hydro: A High-Resolution Global Hydrography Map Based on Latest Topography Dataset,
1107 *Water Resour Res*, 55, 5053–5073, <https://doi.org/10.1029/2019wr024873>, 2019.
- 1108 Yang, C. and Zhao, S.: A building height dataset across China in 2017 estimated by the spatially-
1109 informed approach, *Sci Data*, 9, 76, <https://doi.org/10.1038/s41597-022-01192-x>, 2022.
- 1110 Yuan, H., Dai, Y., Xiao, Z., Ji, D., and Shangguan, W.: Reprocessing the MODIS Leaf Area
1111 Index products for land surface and climate modelling, *Remote Sens Environ*, 115, 1171–1187,
1112 <https://doi.org/10.1016/j.rse.2011.01.001>, 2011.
- 1113 Yuan, X., Ji, P., Wang, L., Liang, X., Yang, K., Ye, A., Su, Z., and Wen, J.: High-Resolution
1114 Land Surface Modeling of Hydrological Changes Over the Sanjiangyuan Region in the Eastern
1115 Tibetan Plateau: 1. Model Development and Evaluation, *J Adv Model Earth Sy*, 10, 2806–2828,
1116 <https://doi.org/10.1029/2018ms001412>, 2018.
- 1117 Zeng, X., Shaikh, M., Dai, Y., Dickinson, R. E., and Myneni, R.: Coupling of the Common Land
1118 Model to the NCAR Community Climate Model, *J Climate*, 15, 1832–1854,
1119 [https://doi.org/10.1175/1520-0442\(2002\)015<1832:cotclm>2.0.co;2](https://doi.org/10.1175/1520-0442(2002)015<1832:cotclm>2.0.co;2), 2002.
- 1120 Zhao, M., Cheng, C., Zhou, Y., Li, X., Shen, S., and Song, C.: A global dataset of annual urban
1121 extents (1992–2020) from harmonized nighttime lights, *Earth Syst Sci Data*, 14, 517–534,
1122 <https://doi.org/10.5194/essd-14-517-2022>, 2022.

1123 Zhou, Y., Li, D., and Li, X.: The Effects of Surface Heterogeneity Scale on the Flux Imbalance
1124 under Free Convection, *J Geophys Res Atmospheres*, 124, 8424–8448,
1125 <https://doi.org/10.1029/2018jd029550>, 2019.